Haematopoietic stem cells in perisinusoidal niches are protected from ageing

Mehmet Saçma[1§], Johannes Pospiech[1§], Ruzhica Bogeska[2], Walter de Back[3], Jan-Philipp Mallm[4], Vadim Sakk[1], Karin Soller[1], Gina Marka[1], Angelika Vollmer[1], Rebekah Karns[5], Nina Cabezas-Wallscheid[6], Andreas Trumpp[2], Simón Méndez-Ferrer[7,8], Michael D. Milsom[2], Medhanie A. Mulaw[9], Hartmut Geiger[1,10], Maria Carolina Florian*[1, 11]

[1]Institute of Molecular Medicine, Stem Cells and Aging, Aging Research Center, Ulm University, Ulm, Germany

[2]Heidelberg Institute for Stem Cell Technology and Experimental Medicine gGmbH (HI-STEM) and Deutsches Krebsforschungszentrum (DKFZ), Division of Experimental Hematology, Heidelberg, Germany

[3]Institute for Medical Informatics and Biometry, Faculty of Medicine Carl Gustav Carus, Technische Universität Dresden, Germany

[4]Deutsches Krebsforschungszentrum (DKFZ), Division of Chromatin Network, Heidelberg, Germany

[5]Division of Gastroenterology, Hepatology, and Nutrition, Cincinnati Children's Hospital Medical Center and University of Cincinnati, Cincinnati, OH, USA

[6]Max Planck Institute (MPI) of Immunobiology and Epigenetics, Freiburg, Germany

[7]Wellcome Trust-Medical Research Council Cambridge Stem Cell Institute and Department of Hematology, University of Cambridge, Cambridge, United Kingdom

[8]National Health Service Blood & Transplant, Cambridge Biomedical Campus, Cambridge, United Kingdom

[9]Molecular Oncology Institute of Experimental Cancer Research, Medical Faculty, University of Ulm, Albert-Einstein-Allee 11, D-89081 Ulm, Germany

[10]Division of Experimental Hematology and Cancer Biology, Cincinnati Children's Hospital Medical Center and University of Cincinnati, Cincinnati, OH, USA

[11]Center for Regenerative Medicine in Barcelona (CMRB), Barcelona, Spain

§first co-authors

*Correspondence to: M. Carolina Florian, Center for Regenerative Medicine in Barcelona (CMRB), Barcelona, Spain or Institute of Molecular Medicine and Stem Cell Aging, University of Ulm, Germany;

e-mail: cflorian@cmrb.eu or carolina.florian@uni-ulm.de; phone: +34 93 316 0304 or +49 731 5026712

Summary

With ageing, intrinsic hematopoietic stem cell (HSC) activity decreases, resulting in impaired tissue homeostasis, reduced engraftment following transplantation and increased susceptibility to diseases. However, whether ageing affects also the HSC niche impairing its capacity to support HSC function is still largely debated.

Here, by using *in-vivo* long-term label retention assays we demonstrate that aged labelling retaining (LR) HSCs, which are in the old mice the most quiescent HSC subpopulation with the highest regenerative capacity and cellular polarity, reside predominantly in perisinusoidal niches. Furthermore, we demonstrate that sinusoidal niches are uniquely preserved in shape, morphology and number upon ageing. Finally, we show that myeloablative chemotherapy can selectively disrupt aged sinusoidal niches long term, which is linked to to the lack of recovery of endothelial Jag2 at sinusoids.

Overall, our data characterize the functional alterations of the aged HSC niche and unveil that perisinusoidal niches are uniquely preserved and protect HSCs from ageing.

Introduction

Bone marrow (BM) HSC niches are composed of multiple haematopoietic and non-haematopoietic cells interacting in a complex 3-dimensional (3D) architecture to support HSC function[1-12]. Upon ageing, HSC activity decreases, resulting in impaired tissue homeostasis, reduced engraftment following transplantation and increased susceptibility to diseases and leukemia[13-18]. Changes of the HSC niche upon ageing might also affect stem cell activity[19].

Here, to functionally characterize the interaction between BM niches and HSCs upon ageing, we employed SCL-tTAxH2B-GFP double heterozygous mice to identify aged HSCs able to retain the pulsed histone 2B-green fluorescent protein (H2BGFP) label *in vivo* after at least 18 months of chase (**Fig. 1a**; aged labelling retaining HSCs, aLR-HSCs). LR-HSCs were shown to act as a reserve stem cell population resisting chemotherapeutic challenge[20-25]. We demonstrate that in aged mice LR-HSCs reside predominantly in sinusoidal niches and are functionally and phenotypically younger than non-LR HSCs. We show that upon ageing HSCs are located more distant to multiple types of bone marrow niche cells but not from sinusoids and

55 perisinusoidal Nestin(Nes)-GFP^{low} cells. Sinusoidal niches and Nes-GFP^{low} cells remain uniquely preserved in
56 shape, morphology and number upon ageing. We show that Jag2 is expressed at sinusoids and perisinusoidal
57 Nes-GFP^{low} cells in proximity to aLR-HSCs, and that blocking endothelial Jag2 promotes HSC proliferation.
58 Finally, we demonstrate that myeloablative chemotherapy disrupts the function of aged sinusoidal niches long-
59 term, which is linked to the lack of recovery of endothelial Jag2 at sinusoids after chemotherapy and results in
60 haematopoietic failure and decreased survival of aged mice.

61 Overall, our data characterize the divergence in niche preservation of HSC function during ageing and
62 unveil that perisinusoidal niches are uniquely protected, supporting aLR-HSCs located in their proximity.
63 These findings underlie that physiological alterations of the BM niche upon ageing impact on haematopoiesis
64 and survival particularly in the context of specific (chemo-)therapeutic interventions.

65

66 **Results**

67 **Aged LR-HSCs are located in proximity to sinusoids.**

68 At 20 months of age, after 18 months of continuous doxycycline (DOX) chase, 0.0057 ± 0.0013% of BM cells
69 were LR-HSCs (gated as Lin$^-$Kit$^+$Sca-1$^+$Flk2$^-$CD34$^-$CD48$^-$CD150$^+$H2B-GFP$^+$) (**Supplementary Fig. 1a-d**).
70 Notably, the ageing-associated expansion of LR-HSCs was relatively modest (~3-fold) compared to ~11.8-
71 fold expansion of aged GFP$^-$ non-LR-HSCs (anLR-HSCs) (**Supplementary Fig. 1e**). Based on single aLR-
72 HSC transplantation assays into *Rag2*$^{-/-}$*γc*$^{-/-}$*Kit*$^{W/Wv}$ recipient mice[26], more than 80% of these cells were
73 functional long-term HSCs (**Supplementary Fig. 1f-h**). Both aLR-HSCs and anLR-HSCs reconstituted hosts
74 up to secondary transplants. However, aLR-HSCs demonstrated >8-fold higher engraftment in blood and a
75 tendency to increased reconstitution of the stem and progenitor pool when compared to anLR-HSCs in both
76 primary and secondary recipients, with no differences in lineage contribution (**Supplementary Fig. 2a-e**).
77 aLR-HSCs were predominantly composed of young-like polar HSCs, whereas anLR-HSCs were largely apolar
78 (**Supplementary Fig. 2f-i**)[19, 27-29]. Therefore, function and phenotypes associated with ageing characterize
79 primarily nLR-HSCs in aged mice.

80 We hypothesized that these "younger" LR-HSCs in the aged BM might be located at selected niches,
81 here defined as 3D-spatial areas of the BM tissue characterized by HSCs and selected cell types lying in

82 proximity to each other (**Fig. 1b**). Young HSCs are found as individual stem cells[30] in proximity to
83 periarteriolar and perisinusoidal cells[1-5] and reside frequently at the endosteal area of the BM cavity[1, 6, 7]
84 associating often also with megakaryocytes (MKs)[8-10]. While young LR- and CD150$^+$ LR-cells were found
85 homogenously throughout the BM and also at the endosteal area, in agreement with previous reports[21], aLR-
86 HSCs were observed always as individual stem cells mostly located close (8.1 ± 1.2 µm) to the vasculature
87 >50µm from the endosteum (**Fig. 1c, f, g** and **Supplementary Fig. 2j-k**). In contrast, anLR-HSCs were found
88 more frequently in clusters[30, 31] and were significantly further from the vasculature (18.5 ± 1.2 µm and 21.7 ±
89 1.0 µm, for single and clustered anLR-HSCs respectively, **Fig. 1d-g**). aLR-HSCs were found almost
90 exclusively (83%) located in proximity to sinusoids, while only 19 % and 10% of single and clustered anLR-
91 HSCs were at sinusoids (**Fig. 1h-j and Supplementary Video 1** and **Supplementary Fig. 2l-o** for the
92 histological distinction between sinusoidal and arteriolar vessels). aLR-HSCs and anLR-HSCs weren't located
93 in proximity to both the endosteum and MKs (**Fig. 1k-m**). Therefore, aLR-HSCs are individual stem cells
94 found selectively and specifically in proximity to perisinusoidal niches.
95

96 **Aged HSCs are located more distant to most niche cells, but not to perivascular Nes-GFP^{low}**
97 **cells and sinusoids, which are uniquely preserved upon ageing.**

98 Intrigued by our findings on aLR-HSCs, we performed a more comprehensive characterization of whether the
99 distance of HSCs from niche cells changes with ageing. In the BM endosteal region of young mice HSC
100 frequency was >2-fold higher compared to aged mice and HSCs were significantly more distant from the
101 endosteum (**Fig. 2a-d**, **Supplementary Fig. 3a, Supplementary Table 1**). As previously reported[8, 10], 26 ±
102 2% of HSCs in the young BM were in proximity to MKs, while in the aged setting, only 10.3 ± 2.1% of HSCs
103 were located near to MKs (**Supplementary Fig. 3b-e**). In aged mice, the frequency of HSCs in proximity to
104 Nes-GFP^{high} cells was also significantly reduced, while the frequency of HSCs adjacent to Nes-GFP^{low} cells
105 was unaltered. Therefore, the mean distance of HSCs to the nearest Nes-GFP^{high} cell was increased in old BM,
106 whereas the mean distance to the nearest Nes-GFP^{low} cell was not changed (**Fig. 2e** and **Supplementary Fig.**
107 **3f-k**). Most Nes-GFP^{low} cells were Leptin Receptor$^+$ (LepR$^+$) and the distance of HSCs to perisinusoidal LepR$^+$
108 cells in young and aged BM was similar (**Supplementary Fig. 3l-o**). Furthermore, HSCs were located equally

109 distant to the vasculature in young and old BM, while HSCs in aged mice were more distant from arterioles
110 but not from sinusoids (**Fig. 2f-g, Supplementary Fig. 3p-r** and **Supplementary Video 2-5**). The frequency
111 and localization of Ki67^{+} HSCs in young and aged BM was comparable (**Supplementary Fig. 4a-b** and
112 **Supplementary Table 2**). Thus, HSCs in aged bone marrow lose proximity to multiple niche cells, but not to
113 sinusoids and perisinusoidal Nes-GFP^{low} cells.

114 Next, we investigated the extent to which ageing alters the number and the architecture of the different
115 niche cells. In both central and endosteal BM preparations[7, 12], Nes-GFP^{high} cells were significantly decreased
116 upon ageing, while the frequency of Nes-GFP^{low} cells remained similar (**Fig. 2i-l** and **Supplementary Fig.**
117 **4c**). The number of megakaryocytes (MKs) was increased (**Fig. 2m-n** and **Supplementary Fig. 4d-e**). The
118 frequency of endothelial cells (ECs) in the endosteal area was significantly decreased, even though the overall
119 vasculature volume and the endothelial area occupancy was not altered (**Fig. 2o-r** and **Supplementary Fig.**
120 **4f-h**). Interestingly, the aged epiphyseal/metaphyseal BM vasculature, which is mainly comprised of arteries
121 and arterioles[32], presented with a decreased length and diameter and a disorganized orientation of the vessels
122 in aged BM (**Fig. 2s-v**). The aged BM diaphyseal area, which is located in the central bone and harbors the
123 vast majority of the sinusoidal vessels[32, 33], was not altered in diameter, length and orientation of vessels (**Fig.**
124 **2s, w-y**). Therefore, sinusoidal/Nes-GFP^{low} cells in aged animals, which harbor LR-HSCs (**Fig. 1h**), are
125 selectively not altered with respect to architecture and number upon ageing.

126

127 **HSC proximity to selected niche cells is not random and endothelial Jag2 maintains aged LR-**
128 **HSCs at sinusoids**

129 We performed *in-silico* modelling to investigate the relationship between changes in niche structure, and the
130 decreased HSC proximity upon ageing. First, we simulated the distribution of 10,000 HSCs randomly placed
131 within the BM cavity and calculated the distance between these randomly placed cells and the different niche
132 structures (indicated as "expected" or "*in silico*" samples). The position of the HSCs was randomly simulated
133 on the bases of each specific niche structure (*see Methods for further details*). Second, we compared the
134 simulated random distributions ("expected") with our 3D histological data. Based on this analysis, we could
135 determine that the localization of HSCs is not random in both young and aged BM with respect to all the

136 selected niche cells (**Fig. 3a** and **Supplementary Fig. 4h-k**). Then, we analyzed the changes in distances
137 between expected ("*in-silico*" computationally generated) young and aged samples. For Nes-GFP^{high} cells and
138 the endosteum the increase in *in-silico* predicted distance agrees with the observed histological data, suggesting
139 that the change in HSC distance is due mainly to the systematic changes in structure and/or distribution of
140 these niche cells (**Fig. 3b, d** and **Supplementary Fig 4l-m**). Both the *in-silico* model and the histological data
141 indicated that the distance from Nes-GFP^{low} cells was not altered (**Fig. 3c-d**). With regards to MKs, the model
142 did not predict changes with ageing, indicating that the observed increased distance is not driven by structural
143 changes in MKs (**Fig. 3d** and **Supplementary Fig. 4m**).
144 To further validate the relevance of the HSC position with respect to niche cells, we assessed if we can predict
145 based on the relative distance to various niche cells if a HSC is young or aged. To this aim, we performed a
146 keras/tensorFlow multilayer deep learning analysis based on the 7 different distance measurements of HSCs
147 from vasculature, endosteum, NesGFP^{low}, NesGFP^{high}, Megakaryocytes (MK), LepR^{+}, and distance between
148 HSCs. Though each of these histological measurements were collected on hundreds of cells, not all
149 measurements were done simultaneously for a given cell. To address this in a robust and multivariate manner,
150 we subsampled data from each measurement and merged them into a matrix for every training step of the
151 model (*see Methods for further details*). The model was then sequentially trained for 50 rounds (iterations),
152 each iteration (50 epochs) taking new sampling data of the training set. Validation was done on a subset of
153 data not seen by the model. We observed close to 70% prediction accuracy in the first iteration, which linearly
154 increased to 82.5% after 50 rounds of iteration (**Fig. 3e-f**). To assess the model improvement efficiency with
155 every round of subsampling, we binned the results into 10 groups (each with 5 iterations). A correlation
156 analysis between the median accuracy of the bins and their ordered/ranked version (smallest to largest) was
157 statistically highly significant, indicating that the model significantly and linearly improved over the iterations
158 considered (**Fig. 3e**). When we assessed the confusion table (degree of match between empirical and predicted
159 HSCs), we saw that the model is predicting equally well if a HSC is young or aged and the rate of
160 misclassification in the validation set was comparable (14.8% of mis-classified young HSCs and 18.8% of
161 mis-classified aged HSCs; **Fig. 3f**). In the final step, we looked at the overall relevance of each niche cell type
162 in the prediction analysis. All parameters were positively correlated and there was no significant difference
163 between their correlation coefficients (**Fig. 3g**), indicating that none of the niche cells is individually important

164 but they need to be considered simultaneously (**Fig. 3g** and **Supplementary Fig. 5**). Therefore, according to
165 our deep learning approach the proximity of selected niche cells to HSCs can be successfully used to predict
166 whether a given stem cell is young or old.

167 To additionally support proximity to specific cell types as a critical aspect to characterize whether
168 young and aged niches are functionally different, we performed competitive young and aged HSC transplants
169 into not irradiated young and aged *Rag2*$^{-/-}$*γc*$^{-/-}$*Kit*$^{W/Wv}$ recipient mice (**Fig. 3h**). The histological data and PB
170 data showed that in young recipients, young and aged HSCs localize with significantly different frequency in
171 proximity to arterioles/endosteum compared to sinusoids, while in aged recipients both young and aged HSCs
172 localize with the same frequency at sinusoids (**Fig. 3i-k** and **Supplementary Fig. 6a-f**). Despite the intrinsic
173 difference, both young and aged HSCs function as stem cells (**Supplementary Fig. 6g-h**). Therefore, the data
174 substantiate the *in-silico* model showing that HSC proximity to selected niche cells is not random and at least
175 in young mice, young and aged HSCs are found in different functional niches. In addition, the data indicate
176 that in aged mice the endosteal/arteriolar niche is functionally disadvantaged compared to the sinusoidal niche.

177 Next, we performed single-cell RNA sequencing (scRNA-seq) on aLR-HSCs, that locate almost
178 exclusively at sinusoids (**Fig. 1h** and **Supplementary Fig. 6i**). Similar to our functional data, when analysed
179 together with scRNA-seq dataset from young HSCs[23], LR-HSCs from aged mice were transcriptionally
180 younger than nLR-HSCs (**Fig. 4a).** A total of 1058 genes were up regulated in aLR-HSCs compared to anLR-
181 HSCs**,** including *Cxcr4*[34, 35], *Dek*[36], *Gpr56*[37, 38] and *Ctnnb1* (**Fig. 4b** and **Supplementary Fig. 6j-o** and
182 **Supplementary Table 3**). Consistent with a younger transcriptome in LR-HSCs from aged mice, GO analyses
183 revealed an enrichment for canonical Wnt and cell polarity establishment[27], which are associated with young
184 HSCs[28, 30] (**Fig. 4c**). Of note, there was also increased expression of *Rbpj* and *Hes1* critically linked to canonical
185 Notch signalling[39-41] (**Fig. 4d**). Notch signaling in HSCs is engaged by Jag/Dll ligands on juxtaposed cells and
186 requires cell proximity[42]. Supporting that active Notch signaling might be critical for LR-HSCs proximity at
187 sinusoidal niches, we observed high levels of Jag2 at sinusoids and Nes-GFP^{low} cells in young and especially
188 in aged BM, as well as at sinusoids that were in proximity to aLR cells (**Fig. 4e** and **Supplementary Video**
189 **6**). Jag2 levels were markedly reduced in aged Nes-GFP^{high}/arteriolar cells in aged mice (**Fig. 4f**). Flow
190 cytometry analyses revealed that the frequency of Jag2^{+}Nes-GFP^{low} and Jag2^{+}ECs was preserved in aged mice,
191 while there was a more than 2-fold decrease in the frequency of Jag2^{+}Nes-GFP^{high} cells. The maintenance of

192 Jag2 expression in sinusoids upon ageing was specific to Jag2. For example, Jag1 was found to be significantly
193 reduced in aged sinusoids and endothelium (**Fig. 4g-i** and **Supplementary Fig. 7a-b**). Dll1 and Dll4 were
194 barely detectable and not changed with ageing (**Fig. 4g-i** and *data not shown*). To determine the role of
195 endothelial Jag2 for HSC function, first we performed *in vitro* co-culture experiments. Blocking endothelial-
196 derived Jag2 markedly increased the number and thus proliferation of HSCs (**Supplementary Fig. 7c-f**).
197 Second, we injected the Jag2-blocking antibody directly in aged mice (**Fig. 4j**). In BM, the Jag2-blocking
198 antibody showed a very specific staining pattern similar to the Jag2 distribution detected by histology and flow
199 cytometry analysis, binding mainly aged endothelial sinusoids (**Supplementary Fig. 7g**). Consistently with
200 the *in vitro* data, blocking Jag2 *in vivo* induced in the diaphyseal central BM higher proliferation of aged HSCs
201 and clustering at sinusoids (**Fig. 4k-n** and **Supplementary Fig. 7h**). Overall, in this region the frequency of
202 sinusoidal Ki67^{+} HSCs doubled (**Fig. 4m** and **Supplementary Fig. 7i-j**) and the effect was almost exclusively
203 localized at sinusoids (**Supplementary Fig. 7i-k**), resulting in a significant increase in the frequency of
204 clustered HSCs in proximity to sinusoidal niches (**Supplementary Fig. 7k**), which are normally extremely
205 rare in control condition. In summary, our data show that Jag2 is expressed at sinusoids and by Nes-GFP^{low}
206 cells in aged BM in proximity to aLR-HSCs and that endothelial Jag2 suppresses HSC proliferation and
207 clustering.
208

209 **5-FU treatment specifically disrupts sinusoidal niches and impairs haematopoiesis and survival**
210 **of aged mice**

211 To functionally investigate the sinusoidal niche in aged animals, we performed treatments with 5-fluorouracile
212 (5-FU), which in young mice results in damage to sinusoidal niches as well as myelosuppression[43-45]. The aged
213 sinusoidal niche was also dramatically compromised by 5-FU, with markedly reduced cellularity and increased
214 diameter of the sinusoidal vessels (**Supplementary Fig. 8a** and **Fig. 5a-d**). However, the arterioles and the
215 endosteal niche were largely unaffected by 5-FU, particularly so in the case of aged mice (**Fig. 5d-f**). The
216 sinusoidal disruption correlated with a reduction in Nes-GFP^{low} cells in the aged mice only, whereas Nes-
217 GFP^{high} cells remained unaltered after 5-FU (**Fig. 5g-h**). The percentage of cycling HSCs after 5-FU remained
218 very low in aged mice and we didn't observe clusters of proliferative MPPs. In contrast, 62.7% of HSCs in

219 young 5-FU treated mice were actively cycling (Ki-67$^+$) and we detected numerous clusters of proliferating
220 MPPs. Of note, HSCs from aged mice transplanted in a young niche showed an increase in the frequency of
221 Ki-67$^+$ HSCs after 5-FU, supporting a critical and dominant role of the young niche for the activation of HSCs
222 after myelosuppression (**Fig. 5i-j** and **Supplementary Fig. 8b-c**). While haematopoiesis recovered within 30
223 days of 5-FU treatment, after 4-5 months aged 5-FU treated mice showed a significant decrease in white blood
224 cells associated with a reduction in long-term survival post treatment, suggesting that the HSC compartment
225 may be compromised (**Fig. 5k-l** and **Supplementary Fig. 8d**). To exclude the possibility that 5-FU might
226 directly damage the HSCs, we performed transplantations of young and aged recipient mice preconditioned by
227 5-FU**.** We detected very low/absent engraftment in 5-FU preconditioned young and aged mice, while irradiated
228 recipients (11Gy) were efficiently engrafted. These data indicate that endogenous HSCs in 5-FU
229 preconditioned recipients were not directly affected by the chemotherapy **(Fig. 5m** and **Supplementary Fig.**
230 **8e-f).** Of note, sinusoids remained significantly enlarged in aged mice still 30 days after 5-FU treatment
231 (**Supplementary Fig. 8g-h**)**.** scRNA-seq of sorted young and aged ECs showed largely overlapping
232 transcriptome profiles with few differentially expressed genes, mainly indicating a lack of proliferating ECs
233 within the aged samples **(Supplementary Fig. 8i-k** and **Supplementary Table 4)**. Interestingly, Jag2
234 expression did not recover in the aged sinusoidal niche after 5-FU and HSCs localized significantly farther
235 away from sinusoids, while their proximity to arterioles increased **(Fig. 5n-p).** Considering that we detected
236 no change in the frequency and proliferation rate of HSCs in the aged BM after 5-FU **(Fig. 5j** and
237 **Supplementary Fig. 8l-m)**, we conclude that HSCs likely relocated to the arteriolar niche**.** Since young mice
238 fully recover after 5-FU treatment (**Fig. 5l**) and 5-FU did not directly affect HSCs in both young and aged mice
239 (**Fig. 5m)**, our data strongly support that the Jag2$^+$ sinusoidal niche is critical for maintaining functional HSCs
240 in aged animals.
241

242 **Discussion**

243 Collectively, our data imply that aLR-HSCs, when compared to anLR-HSCs, present with the highest
244 regenerative potential; a less pronounced expansion compared to young cells; an absence of clustering; high
245 cytosol and epigenetic polarity; canonical Wnt signaling; an overall "younger" transcriptome profile. In
246 addition, we show here that aLR-HSCs are exclusively found at sinusoidal niches, that are central for

247 maintaining haematopoiesis in aged mice. Transplantation assays, histological data and *in silico* modelling all
248 convey that the perisinusoidal/Nes-GFP^{low} niche is uniquely phenotypically and functionally preserved upon
249 ageing, while in general most niches and the proximity of HSCs to niche cells are significantly altered upon
250 ageing (**Supplementary Fig. 9a**). To note, according to our deep learning approach the proximity of selected
251 niche cells to HSCs can be successfully used even to predict whether a given stem cell is young or old.
252 In light of a supportive contribution of the niche to the intrinsic function of HSCs[46], our data strongly imply
253 that the sinusoidal/Nes-GFP^{low} niche in aged mice, via Jag2 signaling, preserves a more pristine function of
254 HSCs located close to it. The deficiency in endothelial Jag2 recovery after 5-FU treatment **(Fig. 5n-o)** might
255 be one critical aspect defeating haematopoietic stem cell functional preservation in old mice. These data are
256 surprising when considering previous findings ruling out a significant effect of cell-autonomous canonical
257 Notch signaling on HSC maintenance *in vivo*[47]. However, haematopoietic stress and inflammation, as after 5-
258 FU treatment and ageing, were not directly investigated. Our data are consistent indeed with a more recent
259 report highlighting specifically the importance of endothelial Jag2 after myelosuppression[48]. Collectively,
260 these findings add critically to our understanding of how a specific BM niche can impact on HSC fate in the
261 elderly in general and particularly in the context of specific chemotherapeutic interventions.

262 **Methods**

263 **Mice.** SCL-tTAxH2B-GFP double heterozygous mice bones were obtained from the Milsom's laboratory
264 (Deutsches Krebsforschungszentrum, Division of Experimental Hematology, Heidelberg, Germany).
265 Technical details on mouse DOX treatment were previously described[22]. Nes-GFP transgenic mouse line was
266 obtained from the Méndez-Ferrer's laboratory (Wellcome Trust-Medical Research Council Cambridge Stem
267 Cell Institute and Department of Hematology, University of Cambridge, Cambridge, United Kingdom).
268 C57BL/6 mice (8-16-week-old) were obtained from Janvier. Aged C57BL/6 mice (20-26-month-old) were
269 obtained from the internal divisional stock (derived from mice obtained from both The Jackson Laboratory
270 and Janvier) as well as from NIA/Charles River. $Rag2^{-/-}\gamma c^{-/-}Kit^{W/Wv}$ mice were obtained from the internal
271 divisional stock (derived from mice obtained from Hans-Reimer Rodewald[26]). Young and aged AcRFP and
272 AcYFP mice were obtained from the internal divisional stock (derived from mice obtained from Prof. Hans
273 Joerg Fehling, Institute of Immunology, Ulm University, Germany). Briefly, Pan-YFP mice carrying
274 constitutively active ROSA26-tdYFP alleles (indicated in the manuscript as AcYFP mice) were obtained from
275 Prof. Hans Joerg Fehling (Institute of Immunology, Ulm University) and were previously generated by
276 intercrossing C57BL/6-Gt(ROSA)26Sortm1Hjf/Ieg mice[49] with animals from a germline Cre-deleter strain[50].
277 Offspring in which the ROSA26-driven fluorescent tdYFP reporter had been activated irreversibly as the result
278 of loxP/Cre-mediated recombination in the germline were backcrossed for > 10 generations onto C57BL/6,
279 thereby eliminating the Cre recombinase transgene. AcYFP mice were used as homozygotes. Young AcCFP
280 mice were obtained from the internal divisional stock (derived from mice obtained from Dr. Yi Zheng,
281 Cincinnati Children Hospital Medical Centre, Cincinnati, Ohio, USA). All mice were housed in the animal
282 barrier facility under pathogen-free conditions at the University of Ulm. Throughout the manuscript young
283 mice are between 10 and 16-week-old and aged mice are at least 80-week-old. To induce myeloablation by 5-
284 FU, mice were intraperitoneally administered one dose of 5-FU (150mg/kg). Young mice were treated with
285 5-FU at 10 weeks of age; old mice were treated with 5-FU at 76 week of age. Mice for this study were randomly
286 selected and survival was followed up to 270 days after 5-FU administration. To assess the statistical
287 significance of differences in survival, we performed Log Rank Mantel Cox test. All statistical tests were
288 performed using GraphPad with Prism7, following its Statistics Guide.

289 All mouse experiments were performed in compliance with the German Law for Welfare of Laboratory
290 Animals and were approved by the Institutional Review Board of the University of Ulm.
291
292 **Flow cytometry and cell sorting.** PB and BM cell immunostaining was performed according to standard
293 procedures and samples were analyzed on a LSRII flow cytometer (BD Biosciences). Monoclonal antibodies
294 to Ly5.2 (clone 104, eBioscience) and Ly5.1 (clone A20, eBioscience) were used to distinguish recipient from
295 donor cells. For PB and BM lineage analysis the antibodies used were all from eBioscience: anti-CD3ε (clone
296 145-2C11), anti-B220 (clone RA3-6B2), anti-Mac-1 (clone M1/70) and anti-Gr-1 (clone RC57BL/6-8C5).
297 Lineage FACS analysis data are plotted as the percentage of B220$^+$, CD3$^+$ and Myeloid (Gr-1$^+$, Mac-1$^+$ and
298 Gr-1$^+$ Mac-1$^+$) cells among donor-derived cells in case of a transplantation experiment or among total white
299 blood cells. Gating strategy is according to **Supplementary Fig. 9e**. As for early haematopoiesis analysis,
300 mononuclear cells were isolated by low-density centrifugation (Histopaque 1083, Sigma) and stained with a
301 cocktail of biotinylated lineage antibodies. Biotinylated antibodies used for lineage staining were all rat anti-
302 mouse antibodies: anti-CD11b (clone M1/70), anti-B220 (clone RA3-6B2), anti-CD5 (clone 53-7.3) anti-Gr-
303 1 (clone RB6-8C5), anti-Ter119 and anti-CD8a (Clone 53-6.7) (all from eBioscience). After lineage depletion
304 by magnetic separation (Dynalbeads, Invitrogen), cells were stained with anti-Sca-1 (clone D7) (eBioscience),
305 anti-c-kit (clone 2B8) (eBioscience), anti-CD34 (clone RAM34) (eBioscience), anti-CD127 (clone A7R34)
306 (eBioscience), anti-Flk-2 (clone A2F10) (eBioscience), anti CD48 (clone HM48-1, BioLegend), anti-CD150
307 (clone TC15-12F12.2, BioLegend) and Streptavidin (eBioscience). Early haematopoiesis FACS analysis data
308 were plotted as percentage of long-term haematopoietic stem cells (HSCs, gated as LSK CD34$^{-/low}$ Flk2$^-$ CD48$^-$
309 CD150$^+$), short-term haematopoietic stem cells (ST-HSCs, gated as LSK CD34$^+$ Flk2-) and lymphoid-primed
310 multipotent progenitors (LMPPs, gated as LSK CD34+ Flk2+)[43] distribution among donor-derived LSKs (Lin-
311 c-kit+ Sca-1+ cells). In order to isolate HSCs, lineage depletion was performed to enrich for lineage negative
312 cells. Lineage negative cells were then stained as aforementioned and sorted using a BD FACS Aria III (BD
313 Bioscience).
314 For investigating Notch ligands expression on BM stromal cells, endothelial cells and Nes-GFP$^+$ cells were
315 gated according to **Supplementary Fig. 9b, d**. Additional antibody staining was performed with anti-Jag1
316 APC (clone HMJ1-29 BioLegend), anti-Jag2 eFluor660 (clone HMJ2-1, Invitrogen), anti-Dll1 APC (HMD1-

317 3, BioLegend) and the percentage of positive cells was gated against isotype control (APC Armenian Hamster
318 IgG, BioLegend; eFluor660 Armenian Hamster IgG, ebioscience) stained matching samples.
319
320 **Whole-mount immunofluorescence staining.** After optional i.v. injection of APC-anti-CD31 (clone
321 MEC13.3, BioLegend) and Alexa Fluor® 647-anti-CD144 (clone BV13, BioLegend) antibodies, bones were
322 harvested after post-mortem heart perfusion with 4% paraformaldehyde (PFA) in phosphate-buffered saline
323 (PBS) and were post-fixed in 4% PFA/PBS-solution for 24h at 4°C. Subsequently, bones were embedded
324 without bisecting in optimum cutting temperature compound (O.C.T., Tissue-Tek®) and were snap frozen in
325 liquid nitrogen and stored at -80°C. Bones were shaved along the longitudinal axis on a cryostat until the BM
326 cavity was exposed. The bones were purified from melting O.C.T. Specimens were fixed again in 4% PFA/PBS
327 at RT for 30 minutes. Tissues were blocked and permeabilized with buffer containing 20% donkey serum and
328 0.5% Triton X-100, were incubated with a fluorescently labeled antibody PE-anti-CD150 or Alexa Fluor®
329 488-anti-CD150 (both clone TC15-12F12.2, BioLegend) and Biotin-labeled primary antibodies anti-CD41
330 (clone MWReg30), anti-CD48 (clone HM48-1), anti-CD11b (clone M1/70), anti-B220 (clone RA3-6B2), anti-
331 CD5 (clone 53-7.3) anti-Gr-1 (clone RB6-8C5), anti-Ter-119 and anti-CD8a (Clone 53-6.7) (all from
332 eBioscience) 1-3 days at 4°C and stained with Streptavidin-eFluor®450 (eBioscience), Streptavidin-FITC
333 (eBioscience) or Streptavidin-APC (eBioscience) for 2h at RT. For BM staining, shaved bones were incubated
334 with FITC-anti-Ki-67 (clone SolA15, ebioscience), armenian-hamster-PE-anti-mouse DLL4 (clone HMD4-1,
335 BioLegend), armenian-hamster-PE-anti-mouse DLL1 (clone HMD1-5, ebioscience) or primary antibodies
336 goat-anti-FABP4 (R&D Systems), biotinylated anti-CD41 (clone MWReg30, ebioscience), rabbit-anti-Jag2
337 (clone EPR3646, Abcam) or rabbit-anti-Jag1 (polyclonal, Abcam) 1-2 days at 4°C and stained with secondary
338 antibodies Streptavidin-eFluor®450 (eBioscience) or fluorescently labeled donkey-anti-goat, donkey-anti-
339 rabbit and donkey anti-armenian hamster antibodies (from Jackson ImmunoResearch) for 2h at RT. If
340 necessary, the nuclei were counterstained with DAPI. The fluorescently labeled bone tissues were placed cut-
341 face down onto a 4-well-μ-Slide and were covered in antifade or PBS to prevent tissue desiccation. The
342 preparations were examined under Zeiss LSM 710 or Leica TCS SP8 confocal microscopes and analysed with
343 the image analysis software Volocity (v6.2, Perkin Elmer). The nearest distances from HSCs to multiple niche
344 cell types were measured. The term arteriole includes arterial and arteriolar cell. 2-photon imaging was

345 performed on cryo-shaved long bones using an upright Zeiss 7MP microscope. 2-photon excitation at 800 nm
346 was achieved with a Mai Tai DeepSee Ti:Sa laser (Spectra-Physics) and fluorescence was detected using the
347 BP 500-550 filter to detect green signal (GFP). For second-harmonic generation microscopy a BP485 filter
348 was used to detect blue signal. To visualize the microvasculature, we injected *in vivo* labeled PECAM-1
349 (CD31) and VE-Cadherin (CD144) antibodies or used FABP4 *in situ*[9]. LepR$^+$ cells were stained with anti-
350 mouse Leptin R antibody from R&D Systems AF497. As for the proximity of HSCs to LepR$^+$ cells, we took
351 into consideration only the distance between HSCs and the nearest perivascular LepR$^+$. When it was not
352 possible to match the nearest LepR$^+$ process to an associated perivascular LepR$^+$ cell, we took the nearest
353 perivascular LepR$^+$ cell body. For the Jag2 *in vivo* blocking histological analysis, the images with the highest
354 HSC numbers in the distal-diaphyseal-femoral central BM were taken in consideration.
355
356 **Immunofluorescence staining.** Freshly sorted HSCs were seeded on fibronectin-coated glass coverslips.
357 After culturing cells were fixed with BD Cytofix Fixation Buffer (BD Biosciences). After fixation cells were
358 gently washed with PBS, permeabilized with 0.2% Triton X-100 (Sigma) in PBS for 20 minutes and blocked
359 with 10% Donkey Serum (Sigma) for 30 minutes. Primary and secondary antibodies incubations were
360 performed for 1hr at room temperature. Coverslips were mounted with ProLong Gold Antifade Reagent with
361 or without DAPI (Invitrogen, Molecular Probes). The secondary antibodies for IF were anti-rat DyLight488-
362 conjugated antibody, anti-rat DyLight647-conjugated antibody and anti-rabbit DyLight549-conjugated
363 antibody (all obtained from Jackson ImmunoResearch). Samples were imaged with an AxioObserver Z1
364 microscope (Zeiss) equipped with a 63X PH objective. Images were analysed with Zen software. Alternatively,
365 samples were analysed with an LSM710 confocal microscope (Zeiss) equipped with a 63X objective. Primary
366 raw data were imported into the Volocity Software package (Version 6.2, Perkin Elmer) for further processing
367 and conversion into 3-dimensional images. On average a total of 20 dividing HSCs were singularly analysed
368 per sample. The primary antibodies were anti-alpha tubulin antibody (Abcam, rat monoclonal ab6160) anti-
369 Cdc42 and anti-H4K16ac obtained from Millipore and Abcam (we tested two different antibodies for each
370 target; results were consistent. All 4 antibodies were rabbit polyclonal; anti-Cdc42 from Millipore was
371 previously validated[27, 28]).
372

373 **Endosteal and central BM cell population isolation**. To isolate central BM cells and endosteal BM cells
374 close to the endosteum, femora and tibiae were isolated from young and aged mice. The bones were cleaned
375 and the associated muscle tissues removed. After the bone marrow was flushed out and lysed by RBC buffer
376 (BioLegend) the central BM cells were obtained. The flushed bones were mortared and incubated in 1.5 mg
377 ml collagenase IV (Worthington)/PBS for 1.5 h at 37°C. This endosteal BM cell fraction was filtered through
378 a 70µm cell strainer and counted. Central and endosteal BM cell fractions were stained with CD45.2
379 Monoclonal Antibody (104) PerCP-Cyanine5.5 conjugated (eBioscience), CD31-APC (BioLegend) and
380 CD41-biotinylated+SA-FITC (eBioscience). Gating strategy is according to **Supplementary Fig. 9b-d**.
381
382 **BM endothelial cell culture and HSC-endothelial cell co-culture.** BM endothelial were prepared from
383 young BL6.SJL mice according to[51]. Briefly, after red blood cell lysis, BM cells were seeded on Fibronectin
384 (Takara, 1µg/µl) coated 24-well plates in endothelial Medium: DMEM-HAM's F-12 (Sigma, D6421),
385 20%FBS, 1%P/S, 20mM HEPES, 10µg/ml Heparin, 50µg/ml Endothelial Mitogen (Alfa Aeser #J65416), 5µM
386 SB431542 (R&D, #1614) and cultured at 37°C, 5%CO_2, 3%O_2, with medium change every other day. After 6
387 days of culture, 75-90% of the cells were $CD31^+$ endothelial cells according to FACS-analysis and to cell
388 morphology. For co-culture experiments, 2000-3000 sorted YFP+HSCs (prepared as aforementioned from
389 AcYFP mice) were seeded on top of 6-day cultured BM endothelial cells and the endothelial medium was
390 supplemented with SCF, G-CSF, TPO 100ng/ml each + Jag2 blocking antibody (Bio X Cell BE0125[52],
391 10µg/ml) or Isotype control antibody (eBioscience 14-4888-85, 10µg/ml). HSCs cultured without endothelial
392 cells in the same medium with Jag2 blocking antibody or isotype served as control. After 44-46h of co-culture,
393 cells were harvested and the number of HSCs was assessed by FACS.
394
395 **Preparation of binary vector maps.** The *in silico* simulation was performed based on binary structure maps
396 generated from processed histological data. For this, we prepared whole-mount, long bone marrow sections of
397 young and aged Bl6 mice. We stained for different niche cell populations by immunofluorescent labelling (see
398 corresponding section in Materials & Methods) and recorded confocal images. The z-stack images (z-level
399 depth of 50 µm) were converted to two-dimensional extended-focus representations using the imaging
400 software Volocity. Based on structure-specific immunoflourescent signal and morphology, the images were

401 then cleaned from secondary structures and cells, resulting in binary vector maps containing only the respective
402 niche structure and a structure-free domain (see also **Supplementary Fig. 4h**). For each niche structure, at
403 least three young and three aged maps were analysed, each covering an area of at least 330 x 770 µm with a
404 resolution of at least 3 pixels/µm. The maps were obtained from two animals per niche structure and age group.

405

406 **In silico simulation.** We generated distance distributions, representing the expected distance of HSCs towards
407 the endosteum, NesGFP^{high} cells, NesGFP^{low} cells and MKs in the young and aged setting, under the
408 presumption of random localization and choice of position. For each map we randomly selected 10,000
409 positions in the structure-free domain and recorded the Euclidean distance towards the borders of the respective
410 niche structure. To eliminate boundary artifacts, sampled positions within 25 µm of the map edges were
411 removed and resampled. One representative random distribution was drawn per niche structure and age group
412 by resampling the random distributions calculated for each map of said structure/group for a total of 10,000
413 data points. Those representative random distributions were then used to (i) assess the randomness of
414 localization of HSCs by comparing the observed distances (*in situ*) to the expected random distances (*in silico*).
415 In a second step, we (ii) compared the changes in random distance between young and aged within the *in silico*
416 system. In this way, we were able to assess the systematic effect of structural changes of each isolated niche
417 component, occurring with ageing, and predict changes in distance towards HSCs. The statistical significance
418 of the null hypothesis that both compared distributions are derived from the same statistical population was
419 analysed using two-sample Kolmogorov-Smirnov. The significance levels were set to 0.05 for the comparison
420 observed vs. observed, 1E-3 for observed vs. expected and 1E-8 for expected vs. expected. The effect size D
421 indicates the supremum absolute (vertical) distance between the compared CDFs and is provided for each
422 comparison.

423

424 **Keras/TensorFlow multilayer deep learning.** We employed a keras/TensorFlow binary classification model
425 to predict young and aged HSC based on 7 different distance measurements within the niche. We had an initial
426 layer of 16 units, 3 hidden layers (16 units), and a final output layer of 1 unit (binary output). Glorot uniform
427 initializer was used for kernel initialization while hyperbolic tangent Activation was employed for kernel

428 activation. Stochastic gradient descent (sgd) optimizer was used for model optimization with binary
429 crossentropy loss measurement. The sequential model was trained by sampling data from each parameter (61
430 cases of young and 88 cases of aged for each iteration composed of 50 epochs), and was trained for a total of
431 50 iterations. A total of 80 cases (33 young and 47 aged HSCs) were put aside as a validation set. A bootstrap
432 analysis of the validation set (500 iterations) was later used for the parameter relevance correlation analysis.

433

434 **Single cell RNA preparation (LR-HSCs and nLR-HSCs)**. Single LT-HSCs were sorted based on GFP
435 expression (positive and negative). Cells were cultured overnight without growth factors at 3%O_2 and washed
436 twice with PBS before processing.
437 Single cells were processed using the SMART-Seq v4 Ultra Low Input RNA Kit for Sequencing (Clontech
438 Laboratories, Catalog # 634892) according to manufacturer's instructions. Amplified c-DNA was purified with
439 Agencourt AMPure XP beads (Beckman Coulter, Catalog # A63880) before library preparation with
440 Illumina's NextEra XT DNA Library Preparation kit (Catalog # FC-131-1096) according Illumina's
441 instructions. Library DNA was purified with AMPure XP beads and quantified using Agilent Bioanalyser for
442 manual library normalization. Pooled libraries were subjected to next generation sequencing in Hi-Seq 2500,
443 for pair end 75bp sequencing condition.

444

445 **Single cell RNA preparation ($CD31^+$ endothelial cells)**. Young and aged BM CD45-CD31+ endothelial cells
446 were sorted from endosteal preparations into IMDM (Lonza, Catalog # BE12-722F) + 10% FCS (Sigma). Cells
447 were frozen in IMDM+20%FCS+ 10% DMSO (Sigma). Endothelial cells were thawed, washed once in warm
448 PBS, and subjected immediately to encapsulation in oil droplets using the chromium system by 10X Genomics.
449 cDNA synthesis and library preparation were done according to the manufacturer's instructions for 3' end
450 counting. PCR cycles for both cDNA synthesis and amplification were adjusted for each sample individually
451 to the number of cells loaded cDNA yield respectively. Samples were pooled and sequenced on a HiSeq3000
452 sequencer (Illumina). Five libraries were prepared in three biological replicates.

453

454 **RNA-Sequencing Analysis (LR-HSCs and nLR-HSCs).** Following removal of barcodes and primers, raw
455 reads were aligned to the mm10 mouse genome with annotations provided by UCSC using a proprietary
456 Burrow-Wheeler Transform alignment (COBWeb). Aligned reads were used to compute reads per kilobase
457 per million reads (RPKM) using an EM-algorithm for 38,186 transcripts. Data were normalized using the
458 DESeq algorithm and baselined to the median of all samples. A moderated t-test was used to identify
459 significantly differentially regulated genes between LR-HSCs and nLR-HSCs, with significance set at $p<0.05$
460 and FC>3. Ontological analysis was performed in ToppGene (toppgene.cchmc.org), which gathers data from
461 over 30 ontological repositories. Figures were generated using ToppCluster (toppcluster.cchmc.org) and
462 Cytomap. All data processing and analyses were performed in Strand NGS.
463
464 **RNA-Sequencing Cross-Analysis of aged LR-HSCs and nLR-HSCs vs. young LR-HSCs and HSCs.** Raw
465 alignment data of young LR-HSCs and HSCs published in Cabezas-Wallscheid, N. *et al.*[23] was obtained via
466 the accession number ArrayExpress: E-MTAB-4547. Alignment and lowlevel processing of the data was
467 performed in parallel with our dataset of aged LR-HSCs and nLR-HSCs as described by Cabzeas-Wallscheid
468 *et al.*. Cell filtering on both datasets was performed with reduced stringency (>25,000 reads and >500 detected
469 genes per library). Diffusion map representations of log-transformed, size-factor normalized expression data
470 were generated using the R package destiny[53].
471
472 **RNA-Sequencing Analysis ($CD31^+$ endothelial cells).** UMI counts were generated using the Cell Ranger
473 pipeline (10x Genomics) with default settings and the provided mm10-1.2.0 reference dataset. The cells were
474 filtered based on total number of UMIs (>= 1000), total number of detected genes (>= 1000, at least one read)
475 and percentage of mitochondrial reads (< 10%) using the scater toolkit[54] (R package). Lowly expressed genes
476 were subsequently filtered out (at least 3 reads in 20 different samples). A set of 1651 out of 3384 cells passed
477 all criteria, consisting of 1218 young and 433 aged cells covering 2517 genes. Highly variable genes (HVGs)
478 were identified by using a log-linear fit to capture the relationship between mean and squared coefficient of
479 variation (CV) of log-transformed, size-factor normalized data[55] resulting in 1570 genes. DE analysis was
480 performed on HVGs using DESeq2[56], resulting in 48 genes upregulated with ageing and 11 genes
481 downregulated with ageing. The analysis was performed on raw counts and the likelihood ratio test with the

482 experimental batches as covariables was used. Dispersions were estimated using a local fit and size factors
483 were estimated using the "poscounts" setting. Cell cycle states were scored based on a random forest trained
484 on cell cycle markers genes using Cyclone[57] (implementation in R package scran[58]). Diffusion map
485 representations were generated using the R package destiny[53].
486
487 **Stem cell transplants.** For HSC transplantations in **Supplementary Fig. 2a-e**, aged (20-month-old and 18
488 months under Dox chase) SCL-tTAxH2B-GFP double heterozygous mice (Ly5.1^{+}) were used as donors and
489 Rag2$^{-/-}$γc$^{-/-}$Kit$^{W/Wv}$ mice (Ly5.2^{+}) as recipients. From the same donor mouse 10 LR-HSCs and 10 nLR-HSCs
490 were sorted into separated Terasaki wells. Cells were checked under the microscope before injection into the
491 retro-orbital vein of recipient mice. From each donor mouse 3-4 recipents per each 10 LR-HSCs and 10 nLR-
492 HSCs were transplanted. A total of 4 different donor mice were used for this assay. PB chimerism was
493 determined by FACS analysis at week 4, 12, 16 and 20 post-transplant. The transplantation experiment was
494 performed two times with a cohort of 12-16 recipient mice per group each transplant. After 20 weeks from the
495 primary transplant, total BM from recipient mice was harvested and reinjected into a new cohort of Rag2$^{-/-}$γc^{-}
496 $^{/-}$Kit$^{W/Wv}$ recipient mice. PB chimerism was followed as for primary transplanted mice up to 20 weeks after
497 secondary transplantation.
498 For the single HSC transplantations in **Supplementary Fig. 1f-h**, aged (20-month-old and 18 months under
499 Dox chase) SCL-tTAxH2B-GFP double heterozygous mice (Ly5.1^{+}) were used as donors and Rag2$^{-/-}$γc$^{-/-}$
500 Kit$^{W/Wv}$ mice (Ly5.2^{+}) as recipients. Single HSCs were sorted into Terasaki wells. Cells were checked under
501 the microscope before injection into the retro-orbital vein of recipient mice. A total of 7 recipient mice were
502 used for this assay. PB chimerism was determined by FACS analysis at week 4, 8 and 12 post transplant.
503 For the HSC transplantations in **Fig. 3h**, aged (more than 20-month-old) acYFP and young (10-week-old)
504 acCFP mice were used as donors. 500 HSCs from acYFP and acCFP mice were sorted together in 96 multiwell
505 (1000 HSCs each well). Cells were checked under the microscope before injection into the retro-orbital vein
506 of recipient mice. A total of 5 aged (more than 56-week-old) and 9 young (6-week-old) Rag2$^{-/-}$γc$^{-/-}$Kit$^{W/Wv}$ mice
507 were used as recipients. Young and aged recipient mice were transplanted alongside with the same preparation

508 of 500 CFP+ and 500 YFP+ HSCs. PB chimerism was determined by FACS analysis at week 6, 12 and 16
509 post-transplant.
510 For the HSC transplantations in **Supplementary Fig. 8c**, aged (more than 20-month-old) acYFP mice were
511 used as donors. 500 HSCs from acYFP mice were sorted in 96 multiwell. Cells were checked under the
512 microscope before injection into the retro-orbital vein of recipient mice. A total of 5 young (6-week-old) Rag2$^{-/-}$γc$^{-/-}$Kit$^{W/Wv}$ mice were used as recipients. After 6 weeks from transplant, young recipient mice were injected
514 +/- 5-FU 150mg/kg and 4 days after were sacrificed for histological analysis.
515 For the HSC transplantations in **Supplementary Fig. 8e**, aged (more than 20-month-old) acYFP and young
516 (10-week-old) acYFP mice were used as donors. 500 HSCs from acYFP young and aged mice were sorted in
517 96 multiwell (500 HSCs each well). Cells were checked under the microscope before injection into the retro-
518 orbital vein of recipient mice. A total of 5 aged (more than 56-week-old) and 9 young (6-week-old) Rag2$^{-/-}$γc$^{-/-}$Kit$^{W/Wv}$ mice were used as recipients. Young (12-week-old) and aged (80-week-old) recipient C57Bl6 mice
520 were transplanted after either 11Gy irradiation, 4-day-5-FU injection or no pre-conditioning. Young HSCs
521 were transplanted into young recipients and aged HSCs were transplanted into aged recipients. PB chimerism
522 was determined by FACS analysis at week 3, 6, 9 and 12 post-transplant.
523
524 **Statistical analysis.**
525 All data are plotted as mean ± standard error (s.e.m.). A paired Student's *t*-test was used to determine the
526 significance of the difference between means of two groups. One-way ANOVA or two-way ANOVA were
527 used to compare means among three or more independent groups. The variance was similar between groups
528 that were statistically compared. Distance analysis data were analyzed using a Mann-Whitney U test when
529 non-Gaussian distribution was observed (tested by Shapiro-Wilk and D'Agostino-Pearson omnibus test).
530 Bonferroni post-test to compare all pairs of data set was determined when overall P-value was < 0.05. All
531 statistical analyses were determined with Prism 7.0 version. In each figure legend, the number (n) of biological
532 repeats included in the final statistical analysis is indicated. Mice for experiments were randomly chosen from
533 our in-house colonies or suppliers.

534 **References**

535 1. Kunisaki, Y. *et al.* Arteriolar niches maintain haematopoietic stem cell quiescence. *Nature*
536 **502**, 637-643 (2013).
537 2. Ding, L., Saunders, T.L., Enikolopov, G. & Morrison, S.J. Endothelial and perivascular cells
538 maintain haematopoietic stem cells. *Nature* **481**, 457-462 (2012).
539 3. Acar, M. *et al.* Deep imaging of bone marrow shows non-dividing stem cells are mainly
540 perisinusoidal. *Nature* **526**, 126-130 (2015).
541 4. Itkin, T. *et al.* Distinct bone marrow blood vessels differentially regulate haematopoiesis.
542 *Nature* **532**, 323-328 (2016).
543 5. Chen, J.Y. *et al.* Hoxb5 marks long-term haematopoietic stem cells and reveals a homogenous
544 perivascular niche. *Nature* **530**, 223-227 (2016).
545 6. Calvi, L.M. *et al.* Osteoblastic cells regulate the haematopoietic stem cell niche. *Nature* **425**,
546 841-846 (2003).
547 7. Guidi, N. *et al.* Osteopontin attenuates aging-associated phenotypes of hematopoietic stem
548 cells. *EMBO J* **36**, 1463 (2017).
549 8. Heazlewood, S.Y. *et al.* Megakaryocytes co-localise with hemopoietic stem cells and release
550 cytokines that up-regulate stem cell proliferation. *Stem Cell Res* **11**, 782-792 (2013).
551 9. Zhao, M. *et al.* Megakaryocytes maintain homeostatic quiescence and promote post-injury
552 regeneration of hematopoietic stem cells. *Nat. Med.* **20**, 1321-1326 (2014).
553 10. Bruns, I. *et al.* Megakaryocytes regulate hematopoietic stem cell quiescence through CXCL4
554 secretion. *Nat. Med.* **20**, 1315-1320 (2014).
555 11. Mendez-Ferrer, S. *et al.* Mesenchymal and haematopoietic stem cells form a unique bone
556 marrow niche. *Nature* **466**, 829-834 (2010).
557 12. Haylock, D.N. *et al.* Hemopoietic stem cells with higher hemopoietic potential reside at the
558 bone marrow endosteum. *Stem Cells* **25**, 1062-1069 (2007).
559 13. Akunuru, S. & Geiger, H. Aging, Clonality, and Rejuvenation of Hematopoietic Stem Cells.
560 *Trends Mol Med* **22**, 701-712 (2016).
561 14. Geiger, H., de Haan, G. & Florian, M.C. The ageing haematopoietic stem cell compartment.
562 *Nat Rev Immunol* **13**, 376-389 (2013).
563 15. Morrison, S.J., Wandycz, A.M., Akashi, K., Globerson, A. & Weissman, I.L. The aging of
564 hematopoietic stem cells. *Nat. Med.* **2**, 1011-1016 (1996).
565 16. Rossi, D.J. *et al.* Cell intrinsic alterations underlie hematopoietic stem cell aging. *Proc Natl*
566 *Acad Sci U S A* **102**, 9194-9199 (2005).
567 17. Kamminga, L.M. *et al.* Impaired hematopoietic stem cell functioning after serial
568 transplantation and during normal aging. *Stem Cells* **23**, 82-92 (2005).
569 18. Beerman, I., Maloney, W.J., Weissmann, I.L. & Rossi, D.J. Stem cells and the aging
570 hematopoietic system. *Curr. Opin. Immunol.* **22**, 500-506 (2010).
571 19. Maryanovich, M. *et al.* Adrenergic nerve degeneration in bone marrow drives aging of the
572 hematopoietic stem cell niche. *Nat. Med.* (2018).
573 20. Bockamp, E. *et al.* Tetracycline-controlled transgenic targeting from the SCL locus directs
574 conditional expression to erythrocytes, megakaryocytes, granulocytes, and c-kit-expressing lineage-
575 negative hematopoietic cells. *Blood* **108**, 1533-1541 (2006).
576 21. Wilson, A. *et al.* Hematopoietic stem cells reversibly switch from dormancy to self-renewal
577 during homeostasis and repair. *Cell* **135**, 1118-1129 (2008).
578 22. Walter, D. *et al.* Exit from dormancy provokes DNA-damage-induced attrition in
579 haematopoietic stem cells. *Nature* **520**, 549-552 (2015).
580 23. Cabezas-Wallscheid, N. *et al.* Vitamin A-Retinoic Acid Signaling Regulates Hematopoietic
581 Stem Cell Dormancy. *Cell* **169**, 807-823 e819 (2017).

24. Essers, M.A. *et al.* IFNalpha activates dormant haematopoietic stem cells in vivo. *Nature* **458**, 904-908 (2009).
25. Bernitz, J.M., Kim, H.S., MacArthur, B., Sieburg, H. & Moore, K. Hematopoietic Stem Cells Count and Remember Self-Renewal Divisions. *Cell* **167**, 1296-1309 e1210 (2016).
26. Waskow, C. *et al.* Hematopoietic stem cell transplantation without irradiation. *Nat Methods* **6**, 267-269 (2009).
27. Florian, M.C. *et al.* A canonical to non-canonical Wnt signalling switch in haematopoietic stem-cell ageing. *Nature* **503**, 392-396 (2013).
28. Florian, M.C. *et al.* Cdc42 activity regulates hematopoietic stem cell aging and rejuvenation. *Cell Stem Cell* **10**, 520-530 (2012).
29. Grigoryan, A. *et al.* LaminA/C regulates epigenetic and chromatin architecture changes upon aging of hematopoietic stem cells. *Genome Biol* **19**, 189 (2018).
30. Florian, M.C. *et al.* Aging alters the epigenetic asymmetry of HSC division *PLOS Biology* (2018).
31. Maryanovich, M., Takeishi, S. & Frenette, P.S. Neural Regulation of Bone and Bone Marrow. *Cold Spring Harb Perspect Med* (2018).
32. Kusumbe, A.P. *et al.* Age-dependent modulation of vascular niches for haematopoietic stem cells. *Nature* **532**, 380-384 (2016).
33. Spencer, J.A. *et al.* Direct measurement of local oxygen concentration in the bone marrow of live animals. *Nature* **508**, 269-273 (2014).
34. Zhang, Y. *et al.* CXCR4/CXCL12 axis counteracts hematopoietic stem cell exhaustion through selective protection against oxidative stress. *Sci Rep* **6**, 37827 (2016).
35. Sugiyama, T., Kohara, H., Noda, M. & Nagasawa, T. Maintenance of the hematopoietic stem cell pool by CXCL12-CXCR4 chemokine signaling in bone marrow stromal cell niches. *Immunity* **25**, 977-988 (2006).
36. Broxmeyer, H.E. *et al.* DEK regulates hematopoietic stem engraftment and progenitor cell proliferation. *Stem Cells Dev* **21**, 1449-1454 (2012).
37. Solaimani Kartalaei, P. *et al.* Whole-transcriptome analysis of endothelial to hematopoietic stem cell transition reveals a requirement for Gpr56 in HSC generation. *J. Exp. Med.* **212**, 93-106 (2015).
38. Holmfeldt, P. *et al.* Functional screen identifies regulators of murine hematopoietic stem cell repopulation. *J. Exp. Med.* **213**, 433-449 (2016).
39. Borggrefe, T. & Oswald, F. The Notch signaling pathway: transcriptional regulation at Notch target genes. *Cell. Mol. Life Sci.* **66**, 1631-1646 (2009).
40. Kojika, S. & Griffin, J.D. Notch receptors and hematopoiesis. *Exp. Hematol.* **29**, 1041-1052 (2001).
41. Guiu, J. *et al.* Hes repressors are essential regulators of hematopoietic stem cell development downstream of Notch signaling. *J. Exp. Med.* **210**, 71-84 (2013).
42. Shimizu, K. *et al.* Binding of Delta1, Jagged1, and Jagged2 to Notch2 rapidly induces cleavage, nuclear translocation, and hyperphosphorylation of Notch2. *Mol. Cell. Biol.* **20**, 6913-6922 (2000).
43. Kopp, H.G., Hooper, A.T., Avecilla, S.T. & Rafii, S. Functional heterogeneity of the bone marrow vascular niche. *Ann. N. Y. Acad. Sci.* **1176**, 47-54 (2009).
44. Kopp, H.G. *et al.* Tie2 activation contributes to hemangiogenic regeneration after myelosuppression. *Blood* **106**, 505-513 (2005).
45. Zhou, B.O. *et al.* Bone marrow adipocytes promote the regeneration of stem cells and haematopoiesis by secreting SCF. *Nat Cell Biol* **19**, 891-903 (2017).
46. Baryawno, N., Severe, N. & Scadden, D.T. Hematopoiesis: Reconciling Historic Controversies about the Niche. *Cell Stem Cell* **20**, 590-592 (2017).

631 47. Maillard, I. *et al.* Canonical notch signaling is dispensable for the maintenance of adult
632 hematopoietic stem cells. *Cell Stem Cell* **2**, 356-366 (2008).
633 48. Guo, P. *et al.* Endothelial jagged-2 sustains hematopoietic stem and progenitor reconstitution
634 after myelosuppression. *J. Clin. Invest.* (2017).
635 49. Luche, H., Weber, O., Nageswara Rao, T., Blum, C. & Fehling, H.J. Faithful activation of an
636 extra-bright red fluorescent protein in "knock-in" Cre-reporter mice ideally suited for lineage tracing
637 studies. *Eur. J. Immunol.* **37**, 43-53 (2007).
638 50. Schwenk, F., Baron, U. & Rajewsky, K. A cre-transgenic mouse strain for the ubiquitous
639 deletion of loxP-flanked gene segments including deletion in germ cells. *Nucleic Acids Res* **23**, 5080-
640 5081 (1995).
641 51. Lis, R. *et al.* Conversion of adult endothelium to immunocompetent haematopoietic stem
642 cells. *Nature* **545**, 439-445 (2017).
643 52. Elyaman, W. *et al.* Notch receptors and Smad3 signaling cooperate in the induction of
644 interleukin-9-producing T cells. *Immunity* **36**, 623-634 (2012).
645 53. Angerer, P. *et al.* destiny: diffusion maps for large-scale single-cell data in R. *Bioinformatics*
646 **32**, 1241-1243 (2016).
647 54. McCarthy, D.J., Campbell, K.R., Lun, A.T. & Wills, Q.F. Scater: pre-processing, quality
648 control, normalization and visualization of single-cell RNA-seq data in R. *Bioinformatics* **33**, 1179-
649 1186 (2017).
650 55. Brennecke, P. *et al.* Accounting for technical noise in single-cell RNA-seq experiments. *Nat*
651 *Methods* **10**, 1093-1095 (2013).
652 56. Love, M.I., Huber, W. & Anders, S. Moderated estimation of fold change and dispersion for
653 RNA-seq data with DESeq2. *Genome Biol* **15**, 550 (2014).
654 57. Scialdone, A. *et al.* Computational assignment of cell-cycle stage from single-cell
655 transcriptome data. *Methods* **85**, 54-61 (2015).
656 58. Lun, A.T., McCarthy, D.J. & Marioni, J.C. A step-by-step workflow for low-level analysis of
657 single-cell RNA-seq data with Bioconductor. *F1000Res* **5**, 2122 (2016).
658

Acknowledgment

We thank Jose A. Cancelas (Cincinnati Children Hospital Medical Center, Cincinnati, Ohio, USA) for advice and critical reading of the manuscript. We thank Prof. Hans Joerg Fehling (Institute of Immunology, Ulm University, Germany) for kindly donating AcRFP and AcYFP mice and Dr. Yi Zheng (Cincinnati Children Hospital Medical Center, Cincinnati, Ohio, USA) for donating AcCFP mice. We thank the core facilities at Ulm University: Angelika Rück (Microscope Facility) for support with confocal and 2-photon microscopy, the Cell Sorting Facility and the Tierforschungszentrum (Animal Facility). Work in the laboratory of M.C.F. was supported by an Emmy Noether Grant (DFG), SFB1074 and FOR2674 (DFG) to M.C.F. M.S. was supported by a PhD Degree Scholarship of the Avicenna-Studienwerk.

Author contributions

MS and MCF performed and analyzed laboratory experiments. MS performed all histological experiments and microscopy analysis. JP conceived the computational model with assistance of WDB and performed bioinformatics analysis of scRNA-seq datasets with support from RK. KS and GM assisted in transplantation procedures, bleeding, supported in cell sorting and flow analysis procedures. AV performed single cell RNA-seq sample preparation, supported in cell sorting and flow analysis procedures and performed in vitro co-culture experiments. VS supervised mouse work and took care of breeding, ageing and preparation of the mice used for experiments. MS and MCF designed and interpreted experiments. JPM prepared scRNA-seq libraries from endothelial cells. NC-W supported with scRNA sequencing. NC-W, AT, MDM and RB supported all the experiments involving SCL-tTAxH2B-GFP double heterozygous mice. MAM developed the deep learning algorithm. HG supported in interpreting experiments and writing the manuscript. SMF supported with Nestin-GFP mice and assisted in interpreting experiments. MS, JP and MCF wrote the manuscript.

Competing Financial interests

The authors declare no competing financial interests.

684 **Figure Legends**

685 **Figure 1**. **Aged LR-HSCs are located in proximity to sinusoids.**

686 **a**, Schematic representation of the experimental setup: SCL-tTAxH2B-GFP mice were treated with DOX for
687 18 months starting at 8 weeks of age. H2B-GFP signal is diluted by division and over time only dormant rarely
688 diving cells retain the label. **b**, Cartoon scheme showing how distances between cells were measured. In
689 immunostained whole-mount bones analyzed by 3D confocal microscopy < 10 µm distance from the HSC
690 centroid defines the proximity: HSCs were considered in proximity to a niche cell when the distance from the
691 centroid of an HSC to the edge of a niche cells was less than 10 µm, thus no cell can be found in-between.
692 HSC radius 5 µm and smallest non-erythroblast BM cell radius >5 µm. **c-e**, Representative confocal whole-
693 mount images of old SCL-tTAxH2B-GFP humeral BM showing GFP^+ $CD150^+$ $CD41^-$ $CD48^-$ Lin^- single LR-
694 HSC (**c**), single GFP^- $CD150^+$ $CD41^-$ $CD48^-$ Lin^- nLR-HSC (**d**) and clustered nLR-HSCs (**e**) (arrowheads). LR-
695 HSCs maintain H2B-GFP^+ nuclei (green). Vasculature is stained with FABP4 (magenta). HSCs stain positive
696 for CD150 (red) but negative for all the other haematopoietic markers (CD41, CD48 and lineage are in grey).
697 **f**, Pie chart depicting percentage of single or clustered nLR-HSCs and LR-HSCs present in humeral whole-
698 mount images. **g**, Mean distance of single LR-HSCs and single or clustered nLR-HSCs to the nearest
699 vasculature. **h**, Percentage of single LR-HSCs, single and clustered nLR-HSCs in proximity (< 10 µm) to
700 sinusoids (83.33%, 19.08%, 9.46%), arterioles/arteries (5.56%, 9.21%, 0.00%) and MKs (27.78%, 19.33%,
701 5.33%). **i**, Representative 3D reconstruction of confocal whole-mount images of old SCL-tTAxH2B-GFP
702 humeral BM showing a $CD150^+$ $CD41^-$ $CD48^-$ Lin^- LR-HSC (arrowhead) in proximity to sinusoidal
703 vasculature. **j**, Pie chart showing percentage of the different HSC types which are adjacent to sinusoids (< 10
704 µm, 29%, 57%, 14%). **k**, Mean distance of single LR-HSCs and single or clustered nLR-HSCs to the nearest
705 endosteum. **l**, Mean distance of single LR-HSCs and single or clustered nLR-HSCs to the nearest MK. **m**,
706 Confocal whole-mount images depicting a LR-HSC (arrowhead) in proximity to a MK. In **f-h**, and **j-l**, $n = 245$
707 total HSCs from 6 mice, 51 longitudinal shaved humeral and femoral cross-section areas, 7 biological repeats.
708 Data represent mean ± s.e.m. In **g**, **k**, **l** the statistical significance was assessed by Mann-Whitney-test. * $p <$
709 0.05, ** $p < 0.01$, *** $p < 0.001$, **** $p < 0.0001$. Scale bars 20 µm. See also **Supplementary Figure 1**, **2**
710 and **Supplementary Video 1**.

711

712 **Figure 2. Aged HSCs are located more distant to most niche cells, but not to Nes-GFP^{low} cells and**
713 **sinusoids, which are uniquely preserved upon ageing.**
714 **a**, **b**, Representative 3D confocal whole-mount images of longitudinally shaved C57BL/6 (WT) young (**a**) and
715 old (**b**) femoral BM showing CD150^{+} (red) CD41^{-} CD48^{-} Lin^{-} (white) HSCs in the endosteal area. Vasculature
716 is stained i.v. with anti-PECAM1 and anti-VE-Cadherin (CD31 and CD144, blue) antibodies. Dashed lines
717 denote the endosteum, arrows (yellow) show HSCs. **c**, Percentage of HSCs in the young and old femoral
718 endosteal area (< 50 µm). **d**, Mean distance of HSCs to the young and old femoral endosteum (**c**, **d**, *n* = 232
719 young HSCs from 56 areas and *n* = 495 old HSCs from 30 areas, 6 mice per group). **e**, Percentage of young
720 and old HSCs in direct contact to Nes-GFP^{low} cells (< 10 µm) (*n* = 84 young HSCs from 7 areas and *n* = 135
721 old HSCs from 5, 3 mice per group). **f**, 3D confocal whole-mount images of young and old femoral WT BM.
722 Arrowheads show arterioles, arrows HSCs. Percentage of young and old HSCs adjacent to arterioles (< 10
723 µm). **g**, 3D confocal whole-mount images of young and old femoral WT BM showing spatial relationship of
724 HSCs (arrows) and sinusoids (blue). Percentage of young and old HSCs adjacent to sinusoids (< 10 µm), (**f**, **g**,
725 *n* = 193 young HSCs from 39 areas and *n* = 397 old HSCs from 17 areas, 3 mice per group). **i**, **j**, Pie charts
726 depicting percentage of endosteal and central BM isolated CD45^{-} CD31^{-} Nes-GFP^{+} cells from young and old
727 Nes-GFP mice. **k**, Frequency of CD45^{-} CD31^{-} Nes-GFP^{high} or Nes-GFP^{low} cells among nucleated cells from
728 endosteal and central BM from young and old Nes-GFP mice (**i**-**k** *n* = 4 mice per group). **l**, Representative tile
729 scanned and stacked whole-mount images of tibiae from young and old Nes-GFP mice. **m**, Frequency of
730 CD41^{+} FSC^{high} MKs from young and old WT BM (*n* = 3-4 mice per group). **n**, Quantification of CD41^{+} MKs
731 in z-stacked whole-mount images acquired from young and old long bones (*n* = 7 young and 9 aged
732 longitudinal shaved cross-section areas, two mice per group). **o**, Frequency of CD45^{-} CD31^{+} ECs from young
733 and old WT endosteal BM (*n* = 4 mice per group). **p**, Schematic of a long bone showing epiphysis, metaphysis
734 and diaphysis. (**q**) Epiphyseal/metaphyseal and (**r**) diaphyseal BM areas occupied by vasculature in young and
735 old long bones (*n* = 3/9 and 3/13 areas, 3 mice per group). **s**, Whole-mount images showing vasculature (red)
736 in tibial epiphysis/metaphysis and diaphysis from young and old mice. **t**-**y**, Quantification of
737 epiphyseal/metaphyseal (**t**-**v**) and diaphyseal (**w**-**y**) BV diameter, length and orientation to the bone long axis
738 (*n* = 96/296 young and *n* = 293/418 old BVs from 4-5 epiphyseal/diaphyseal areas, two mice per group). Data
739 represent mean ± s.e.m. In **d** the statistical significance was assessed by Mann-Whitney-test in **c**, **e**, **f**, **g**, **m**, **n**,

740 **o**, **q**, **r**, **t-y** by Student's *t-tests* and in **k** by two-way-ANOVA-test. * $p < 0.05$, ** $p < 0.01$, *** $p < 0.001$, ****
741 $p < 0.0001$, n.s.= not significant. *n* = 2-3 biological repeats. Scale bars, 50 µm (**a**, **b**); 20 µm (**f**, **g**); 500 µm (**l**);
742 100 µm (**s**). See also **Supplementary Figure 3**, **4, Supplementary Table 1, 2** and **Supplementary Video 2-**
743 **5**.
744
745 **Figure 3. HSC proximity to selected niche cells is not random. In young mice, transplanted HSCs lodge**
746 **in at least two different functional niches, while in the aged the endosteal/arteriolar niche is functionally**
747 **impaired.**

748 **a**, Observed (*in situ*) and expected (*in silico*) distances of HSCs towards the endosteum in young and aged
749 mice. Statistical difference indicates a non-random distribution of HSCs in the *in situ* setting. **b, c**, Comparison
750 of distances of HSCs towards Nes-GFP^{low} cells (**b**) or Nes-GFP^{high} cells (**c**) in young and aged mice, within the
751 *in situ* or *in silico* setting. For NesGFP^{low} cells, both observed and expected/random distance distributions show
752 an increase in distance with ageing, while there is no shift in distance for Nes-GFP^{high} cells. For simulation
753 procedure and statistical analysis see *Materials & Methods*. **d**, Summary of changes in distance of HSCs
754 towards different niche structures as observed *in situ* and as predicted by the computational model. **e**, Diffusion
755 map representation of normalized gene expression data of aged LR-HSCs, aged LR-HSCs, young LR-HSCs
756 and young HSCs (young data reanalyzed from[23]). **e**, Summary of the keras/TensorFlow deep learning analysis.
757 Top-right panel: Validation prediction accuracy (y-axis) of the sequential model over 50 iterations (x-axis).
758 Top-left panel: boxplot showing prediction accuracy after summarizing the 50 iterations by binning them into
759 10 groups (5 iterations per bin). Middle-left panel: Median accuracy of the 10 groups are shown. Dotted line
760 depicts a fitted linear model. Middle-right panel: Median accuracy of the ten groups (x-axis) are plotted against
761 a sorted/ranked version. The dotted line shows a linear model recapitulating the significant linear increment of
762 the model over the 50 iterations. Lower-left panel: boxplot showing overall accuracy of the model. Lower-
763 right panel: frequency distribution of the validation accuracy. **f**, Graphical representation of the confusion
764 matrix where correctly classified (blue points) and misclassified (red points) HSCs are shown. Measured (Real
765 class) represents empirical data membership while predicted (y-axis) represents the membership as determined
766 by the keras/TensorFlow deep learning model. We observed an overall 82.5% prediction accuracy. **g**,

767 Correlation analysis showing relevance of the parameters to the classification model. The plots were generated
768 after performing a bootstrap analysis (500 iterations) of correlation coefficient estimation. There was no
769 significant difference between the parameters' correlation coefficients. **h**, Scheme of the competitive BM
770 transplantation experiment of CFP^+ young and YFP^+ aged HSCs into young and aged *Rag2*$^{-/-}$*γc*$^{-/-}$*Kit*$^{W/Wv}$
771 recipient mice. **i**, **j**, Representative 3-dimensional confocal pictures of whole-mount femurs from young (**i**) and
772 aged (**j**) recipient mice transplanted with CFP^+ young and YFP^+ aged HSCs. Donor-derived CFP^+ young HSCs
773 are indicated by cyan and donor-derived YFP^+ aged HSCs by yellow arrowheads. Dashed lines denote the
774 endosteum of the recipient (in **i** 1 unit = 45.23 μm, in **j** 1 unit = 45.72 μm). **k**, Relative distribution of CFP^+
775 young and YFP^+ old HSCs to the endosteum in bones of young and old recipients. (**i**, *n* = 210 CFP^+ young and
776 *n* = 30 YFP^+ old HSCs from 31 areas, two mice per group; **j**, *n* = 80 CFP^+ young and *n* = 27 YFP^+ old HSCs
777 from 30 areas HSCs, two mice per group). *n* = 2-4 biological repeats. See also **Supplementary Figure 4**, **5, 6**
778 and **Supplementary Video 6**.
779
780 **Figure 4. Jag2 maintains aged LR-HSCs at sinusoids.**

781 **a**, Diffusion map representation of normalized gene expression data of aged LR-HSCs, aged LR-HSCs, young
782 LR-HSCs and young HSCs (young data reanalysed from[23]). **b**, Heatmap showing the relative expression levels
783 of 1058 differentially expressed genes (rows) between aged nLR-HSCs and aged LR-HSCs (columns). **c**, GO
784 (gene ontology) analysis of genes that are upregulated in LR-HSCs (detected using ToppGene). **d**, *Rbpj* and
785 *Hes1* are upregulated in LR-HSCs. Values related to single cells and referred to DESeq-normalized and
786 baselined log(FPKM). Data are plotted as average population expression ±SD. **e**, Z-stacked IF images showing
787 Jag2 expression (red) in sinusoidal vessels (blue) and perisinusoidal Nes-GFP^{low} cells (green) in central
788 diaphyseal BM from young and old WT mice. **f**, Representative 3D confocal immunostaining of arteriolar
789 (blue, CD31/CD144) and periarteriolar Nes-GFP^{high} cells (green) of young and old WT endosteal BM showing
790 Jag2 (red) signal (1 unit = 5.48 μm). **g-i**, Percentages of Nes-GFP^{high} cells (**g**), Nes-GFP^{low} cells (**h**) and
791 endothelial cells (**i**) expressing Dll1, Jag1 and Jag2 from young and old Nes-GFP mice (*n* = 2-5 mice per
792 group). **j**, Cartoon scheme depicting the experimental set up. Aged mice were injected twice 24-hour apart
793 with 15mg/kg of either Jag2 blocking antibody or isotype control antibody. 48 hours after the first injection,

794 mice were harvested and processed for whole mount histological analysis. **k**, Z-Stacked confocal images of
795 distal-diaphyseal-femoral central BM from mice treated with Jag2 blocking antibody and isotype control
796 antibody. Scale bars, 100 µm. **l**, Percentage of clustered HSCs in cluster imaged in distal-diaphyseal-femoral
797 central BM whole-mount preparations of mice treated with Jag2 blocking antibody and isotype control
798 antibody showing HSCs (CD150+ in red and exclusion markers CD48, CD41, LIN in white, n = 1265 and n =
799 109 HSCs from 4 and 3 areas; 3 aged mice/group). **m**, Percentage of Ki-67^{+} HSCs present in distal-diaphyseal-
800 femoral central BM whole-mount images of Jag2 blocking antibody and isotype control antibody treated aged
801 mice (n = 966 and n = 109 HSCs per group from 3 areas per group; 2/3 mice/group). **n**, Percentage of clustered
802 HSCs in proximity to sinusoids (< 10 µm) in distal-diaphyseal-femoral central BM whole-mount images of
803 mice treated with Jag2 blocking antibody and isotype control antibody (n = 1113 and n = 109 HSCs from 4
804 and 3 areas, 3 mice/group). In **g-i** and **l-n** data represent mean ± s.e.m and the statistical significance was
805 assessed by Student's *t-tests*. * $p < 0.05$, ** $p < 0.01$. *n* = 2-5 biological repeats. Scale bars, 20 µm (**e**). See
806 also **Supplementary Figure 4**, **5, 6** and **Supplementary Video 6**.
807
808 **Figure 5**. **5-FU treatment specifically disrupts sinusoidal niches and impairs haematopoiesis and**
809 **survival of aged mice.**
810 **a**, Z-stacked whole-mount images showing vasculature (red), nucleated cells (4′,6-diamidino-2-phenylindole,
811 DAPI) and erythroid cells (green) in long bones from young and old mice 4 days after 5-FU administration
812 and non-treated controls. Endosteal BM (eBM) < 50 µm and central BM (cBM) ≥ 50µm from the endosteum
813 (dashed line). **b**, **c**, Quantification of (**b**) BV diameter and (**c**) total nucleated cell (NC) numbers per volume in
814 stacked images in central BM (≥ 50 µm from endost) from 5-FU treated (4d) and non-treated young and old
815 mice (means of (**b**) *n* = 135/81/151/85 BVs from 3 areas, two mice per group). **d**, Images showing arterioles
816 (yellow arrowheads) and sinusoids (blue arrowheads) in BM from 5-FU treated and non-treated young and old
817 mice; CD31/CD144 (red). **e**, **f**, Quantification of (**e**) BV diameter and (**f**) total nucleated cell (NC) numbers
818 per volume in z-stacked images in endosteal BM (< 50 µm from endost) from 5-FU treated (4d) and non-
819 treated young and old mice (means of (**e**) *n* = 46/35/48/36 BVs from 3 areas, two mice per group). **g**,
820 Representative flow density plot of old control and 5-FU treated Nes-GFP cells. **h**, Percentage of absolute
821 number of Nes-GFP^{low} and Nes-GFP^{high} cells in BM of 5-FU treated young and old mice to control (*n* = 3/4

822 mice per group). **i**, Confocal images of young, old and aged YFP$^+$ HSCs prior transplanted in young *Rag2*$^{-/-}$*γc*$^{-}$
823 $^{/-}$*Kit*$^{W/Wv}$ recipient femoral central BM 4 days after 5-FU treatment. Arrows (yellow) show HSCs (CD150$^+$
824 CD41$^-$ CD48$^-$ Lin$^-$, for the transplanted setting CD150$^+$ YFP$^+$ CD41$^-$ CD48$^-$ Lin$^-$). Ki-67 (green) and YFP
825 (yellow). **j**, pie charts depicting percentage of Ki-67$^+$ and Ki-67$^-$ HSCs present in long bone whole-mount
826 images in BM of young, old and aged YFP$^+$ HSCs prior transplanted in young *Rag2*$^{-/-}$*γc*$^{-/-}$*Kit*$^{W/Wv}$ mice 4 days
827 after 5-FU administration. (**i**, **j**, *n* = 52/193/86 HSCs, 3 mice per group). **k**, **l**, Whole blood cell (WBC in K/µl)
828 count (**k**) and survival (**l**) after 5-FU administration of young and old mice; survival of old control mice is also
829 shown. Old mice after 5-FU administration had median survival of 145 days (*n* = 12 mice each group). **m**,
830 Blood chimerism kinetics of overall engrafted donor-derived cells in transplantations of 5-FU preconditioned,
831 lethally irradiated (11 Gy) and control young and aged recipient mice with young or old YFP$^+$ donor HSCs (*n*
832 = 4-6 mice per group). **n**, Stacked whole-mount images showing vasculature (blue) and Jag2 expression (red)
833 in long bones from young and old mice 30 days after 5-FU administration and non-treated controls. **o**, Ratio
834 of Jag2 signal volume to DAPI signal volume in z-stacked images in BM from 5-FU treated (30d) and non-
835 treated young and old mice (*n* = 16/15/15/14 areas, 2-3 mice per group). **p**, Percentage of HSCs from young
836 and old mice 30 days after 5-FU administration and non-treated controls adjacent to sinusoids, arterioles (< 10
837 µm) and in the endosteal area (> 50 µm) (*n* = 84/84/80 young 5-FU 30d HSCs from 30 areas, *n* = 142/142/156
838 old 5-FU 30d HSCs from 27 areas, *n* = 193/193/232 young HSCs from 39/39/56 areas and *n* = 397/397/495
839 old HSCs from 17/17/30 areas, 3-6 mice per group). In **b**, **c**, **e**, **f**, **h**, **k**, **o**, **p** data represent mean ± s.e.m. In **b**,
840 **c**, **e**, **f**, **h**, **o**, **p** the statistical significance was assessed by Student's *t-tests*, in **k** by two-way-ANOVA-test in **l**
841 by log-rank (Mantel-Cox) test. * $p < 0.05$, ** $p < 0.01$, *** $p < 0.001$, **** $p < 0.0001$, n.s.= not significant.
842 *n* = 2-4 biological repeats. Scale bars, 100 µm (**a**); 20 µm (**d**, **i**); 50 µm (**n**). See also **Supplementary Figure**
843 **7** and **Supplementary Table 4**.
844
845 **Supplementary Figure 1: Aged LR-HSC pool expand less than aged nLR-HSCs and are functional long**
846 **term stem cells.**
847 **a**, Representative FACS dot plots of the gating strategy for LR-HSCs (Lin$^-$ c-Kit$^+$ Sca-1$^+$ Flk2$^-$ CD34$^-$ CD48$^-$
848 CD150$^+$ H2B-GFP$^+$) of young and aged not DOX treated H2B-GFP, and young and aged DOX treated SCL-
849 tTAxH2B-GFP lineage-depleted BM cells and schematic representation of the experimental setups. **b**,

850 Frequency of different HSPC subpopulations, LR-HSCs and nLR-HSCs among BM cells in young and old
851 SCL-tTAxH2B-GFP mice after 2 and 18-months of DOX chase, respectively.
852 **c**, Percentages of young and old LR-HSCs in BM cells in DOX treated SCL-tTAxH2B-GFP mice. **d**, Similar
853 frequency of old LSK CD34$^-$ Flk2$^-$ HSCs and old LSK CD34$^-$ Flk2$^-$ CD48$^-$ CD150$^+$ HSCs among BM cells. **e**,
854 Fold expansion of different HSPC subpopulations, LR-HSCs and nLR-HSCs with ageing. **f**, Experimental
855 setup of single aged LR-HSC transplantation in *Rag2*$^{-/-}$*γc*$^{-/-}$*Kit*$^{W/Wv}$ recipient mouse and gating strategy. **g**, Pie
856 chart showing percentage of functional long-term HSCs among single transplanted aged LR-HSCs. **h**, Blood
857 chimerism kinetics of overall engrafted donor-derived cells and of each donor-derived lineage (B cells, T cells
858 and myeloid cells) with single donor old LR-HSCs. Data represent mean ± s.e.m. In **b-e**, *n* = 4 young and 5
859 aged mice. In **g**, *n* = 7 recipient mice. The statistical significance was assessed by Student's *t-test.* * $p < 0.05$.
860
861 **Supplementary Figure 2: Aged LR-HSCs show higher regenerative capacity and are polar and young**
862 **LR-HSCs are located in central and endosteal BM.**
863 **a**, Scheme of the transplantation experiment setup. **b**, Blood chimerism kinetics of overall engrafted donor-
864 derived cells and of each donor-derived lineage (B cells, T cells and myeloid cells) during primary and
865 secondary transplants with donor old LR-HSCs and donor old nLR-HSCs. **c**, Frequency of old nLR-HSCs and
866 old LR-HSCs donor contribution to total white blood cells (WBCs) in PB in *Rag2*$^{-/-}$*γc*$^{-/-}$*Kit*$^{W/Wv}$ recipient mice.
867 **d**, Frequency of LR- and nLR- LT-HSCs in BM among donor-derived (SCL-tTAxH2B-GFP mice after 18-
868 months of DOX chase) LSK cells in *Rag2*$^{-/-}$*γc*$^{-/-}$*Kit*$^{W/Wv}$ recipient mice. **e**, Percentage of B cells, T cells and
869 myeloid cells among donor derived cells. **f**, Representative single-cell IF images showing the distribution of
870 tubulin (green) and Cdc42 (red), in old LR-HSCs and old nLR-HSCs. Nuclei, DAPI (blue). **g**, Representative
871 3D reconstructed single-cell IF confocal images showing the distribution of H4K16ac (magenta) in old LR-
872 HSCs (polar) and old nLR-HSCs (apolar). Nuclei, DAPI (blue). **h**, **i**, Percentage of polar distribution of Cdc42,
873 H4K16ac and tubulin in (**h**) old LR-HSCs and old nLR-HSCs and in (**i**) young LR-HSCs and young nLR-
874 HSCs (*n* = 68/103 old/young LR-HSCs and 78/84 old/young nLR-HSCs from 4/3 different old/young mice
875 for Cdc42; 104/80 old/young LR-HSCs and 120/82 old/young nLR-HSCs from 4/3 different old/young mice
876 for H4K16ac and 172/118 old/young LR-HSCs and 198/116 old/young nLR-HSCs from 7/5 different

877 old/young mice for Tubulin). **j**, Representative stacked whole-mount images of young SCL-tTAxH2B-GFP
878 femoral BM showing label retaining cells (green) and vasculature (blue). **k**, 3D reconstruction of confocal
879 whole-mount images of young SCL-tTAxH2B-GFP femoral BM showing a $CD150^+$ $H2B\text{-}GFP^+$ LR cell in
880 proximity to arterial vasculature (arrowheads) in the endosteal area. **l**, **m**, Distinction of sinusoids and arterioles
881 in (**l**) FABP4 (red) *in situ* stained and (**m**) CD31/CD144 (red) i.v. stained BM: arterioles (yellow arrowheads)
882 have small diameter with continuous staining (continuous basal lamina) and have parallel orientation to the
883 long axis of the bone, sinusoids (blue arrowheads) present relatively larger diameter with spotted staining
884 (fenestrated basal lamina) and are mostly transverse to the long axis. (**l**) Nuclei, DAPI (blue). **n**, **o**,
885 Colocalization of (**n**) sinusoids and (**o**) arterioles/arteries in FABP4 (green) *in situ* stained and CD31/CD144
886 (red) i.v. stained BM. **c-e**, n = 12-14 initial recipient mice in total from 3 different aged donor mice. The
887 statistical significance was assessed by Student's *t-test.* * $p < 0.05$, ** $p < 0.01$. Scale bars 100 µm (**j**); 20 µm
888 (**k-o**).
889
890 **Supplementary Figure 3: HSC proximity to selected niche cell types is altered upon ageing.**
891 **a**, Distance between young and old HSCs to the nearest endosteum (n = 192 young HSCs from 36 areas and n
892 = 432 old HSCs from 17 areas, 3 mice per group), **b**, Confocal images of young and old whole-mount WT
893 femoral BM showing HSCs (arrows) and MKs. **c**, Percentage of young and old HSCs in direct proximity to
894 MKs (< 10 µm). **d**, Mean distance of young and old HSCs to the nearest MK. **e**, Distance between young and
895 old HSCs to the nearest megakaryocyte (**c-e**, n = 177 young HSCs from 34 areas and n = 163 old HSCs from
896 10 areas, 3 mice per group). **f**, Confocal whole-mount images of young and old sternal Nes-GFP mice BM.
897 Arrows (yellow) show HSCs. Nuclei, DAPI (blue). **g**, Percentage of young and old HSCs in direct contact to
898 $Nes\text{-}GFP^{high}$ cells (< 1 µm). **h**, Mean distance of young and old HSCs to the nearest $Nes\text{-}GFP^{high}$ cell (**g**, **h**, n
899 = 137 young HSCs from 9 areas and n = 275 old HSCs from 5, 3 mice per group). **i**, Mean distance of young
900 and old HSCs to the nearest $Nes\text{-}GFP^{low}$ cell (**i**, n = 84 young HSCs from 7 areas and n = 135 old HSCs from
901 5, 3 mice per group). **j**, **k**, Distance between young and old HSCs to the nearest (**j**) $Nes\text{-}GFP^{high}$ cell (n = 137
902 young HSCs from 9 areas and n = 275 old HSCs from 5 areas) and (**k**) $Nes\text{-}GFP^{low}$ cell (n = 84 young HSCs
903 from 7 areas and n = 135 old HSCs from 5 areas) (3 mice per group). **l**, Whole-mount confocal images revealing
904 the overlap of perivascular LepR+ cells (red) and Nes-GFPlow cells (green) surrounding sinusoidal vessels

905 (blue) in central BM of Nes-GFP mice. **m**, Percentage of young and old HSCs adjacent to perivascular LepR+
906 cells (< 10 µm). **n**, Mean distance of young and old HSCs to the nearest perivascular LepR+ cell. **o**, Distance
907 between young and old HSCs to the nearest perivascular LepR+ cell (**m-o**, n = 96 young HSCs from 12 areas
908 and n = 147 old HSCs from 12 areas, two mice per group). **p**, Percentage of young and old HSCs adjacent to
909 BM vasculature (< 10 µm). **q**, Mean distance of young and old HSCs to the nearest vasculature. **r**, Distance
910 between young and old HSCs to the nearest vasculature (**p-r**, *n* = 193 young and *n* = 397 old HSCs, 3 mice
911 per group). Data represent mean ± s.e.m. In **d**, **h**, **i, n**, **q** the statistical significance was assessed by Mann-
912 Whitney-test, in **a**, **e**, **j**, **k**, **n, o, r** the statistical significance was assessed by two-way-ANOVA-test and in **c**,
913 **g**, **m**, **p** by Student's *t-tests*. * $p < 0.05$, ** $p < 0.01$, *** $p < 0.001$, **** $p < 0.0001$, n.s.= not significant. *n* =
914 3 biological repeats. Scale bars, 40 µm (**f**); 20 µm (**b, l**).
915
916 **Supplementary Figure 4: HSC proximity to selected niche cell types is not random.**

917 **a**, Confocal images of WT old femoral BM. Arrow (yellow) shows Ki-67$^+$ (green) HSC. **b**, Pie charts depicting
918 percentage of Ki-67$^+$ and Ki-67$^-$ HSCs (CD150$^+$ CD41$^-$ CD48$^-$ Lin$^-$) present in femoral whole-mount images
919 in BM of WT young and old mice (*n* = 43 young and *n* = 140 old HSCs, 3 mice per group). **c**, 2-photon
920 microscopy images showing Nes-GFP$^+$ cells (green) concentrated at the endosteum of young and aged Nes-
921 GFP mouse BM. Bone (collagen, white) depiction was generated with second-harmonic generation
922 microscopy (1 unit = 13.53 µm). **d**, Representative stacked whole-mount images of WT femoral BM showing
923 CD41$^+$ (yellow) MKs and vasculature (red). **e**, Confocal whole-mount image of WT femoral BM showing
924 perisinusoidal CD41$^+$ (yellow) MKs around sinusoids (red). **f**, Representative 3D reconstruction for volume
925 occupancy measurements of CD31$^+$ CD144$^+$ ECs in femoral whole-mount images. **g**, Epiphyseal/metaphyseal
926 and diaphyseal CD31$^+$ CD144$^+$ ECs volume occupancy in young and old long bone BM (*n* = 3/9 and 3/13
927 areas, 3 mice per group). Data represent mean ± s.e.m. In **g** the statistical significance was assessed by
928 Student's *t-tests*. * $p < 0.05$, n.s.= not significant. *n* = 2-3 biological repeats. Scale bars, 20 µm (**a**, **e**); 100 µm
929 (**d**). **h**, Generation of binary structure maps and depiction of the simulation process. **i-k**, Observed (*in situ*) and
930 expected (*in silico*) distances of HSCs towards Nes-GFP^{high} cells (**i**), Nes-GFP^{low} cells (**j**) or MKs (**k**) in young
931 and aged mice. Statistical difference indicates a non-random distribution of HSCs in the *in situ* setting. **l-m**,

932 Comparison of distances of HSCs towards the endosteum (**l**) or MKs (**m**) in young and aged mice, within the
933 *in situ* or *in silico* setting. With ageing an increase in distance towards the endosteum is both seen *in situ* and
934 predicted by the random model. For MKs an increased distance is observed *in situ*, while the model would
935 predict no alteration. **n**, A representative plot showing a case wise analysis of parameters in either supporting
936 (green) or contradicting (red) that a given sample is aged or young HSC. Case numbers are indicated, along
937 with label (Yes=Aged; No=Young). Model Probability and level of explanation of the fit are also given for
938 each case. For simulation procedure and statistical analysis see Materials & Methods.
939
940 **Supplementary Figure 5: Case wise analysis for old and young HSCs.** A representative plot showing a case
941 wise analysis of parameters in either supporting (green) or contradicting (red) that a given sample is aged or
942 young HSC. Case numbers are indicated, along with label (Yes=Aged; No=Young). Model Probability and
943 level of explanation of the fit are also given for each case.
944
945 **Supplementary Figure 6: In young mice, transplanted HSCs lodge in at least two different functional**
946 **niches, while in the aged the endosteal/arteriolar niche is functionally impaired.**
947 **a,** Confocal images of whole-mount femurs from aged recipient mice transplanted with CFP^+ young and YFP^+
948 aged HSCs. Arrows (white) show donor-derived CFP^+ young and YFP^+ aged HSCs. **b**, Percentage of CFP^+
949 young and YFP^+ old HSCs in young and old recipients adjacent to arterioles, sinusoids and megakaryocytes
950 (< 10 µm) and in the endosteal area (< 50 µm) from femoral whole-mount immunofluorescence images. **c**, **d**,
951 Pie charts depicting percentage of CFP^+ young and YFP^+ old HSCs in the endosteal/arteriolar and
952 sinusoidal/megakaryocytic niche present in long bone whole-mount images of young (**c**) and old (**d**) recipients.
953 **e**, **f**, Relative distribution of CFP^+ young and YFP^+ old HSCs to the endosteum in bones of young (**e**) and old
954 (**f**) recipients. (**c**, **e**, n = 210 CFP^+ young and n = 30 YFP^+ old HSCs from 31 areas, two mice per group; **d**, **f**, n
955 = 80 CFP^+ young and n = 27 YFP^+ old HSCs from 30 areas HSCs, two mice per group). **g**, **h**, Percentage of
956 engraftment, T cells, B cells and myeloid cells from CFP^+ young and YFP^+ aged donor HSCs in peripheral
957 blood of young recipient (**g**) (n = 9 mice each group) and old recipient mice (**h**) (n = 5 mice each group). **i**,
958 Overview of the single cell RNAseq experimental layout. **j-o**, Histone variants (**j**) *H2afz*, (**k**) *H3f3a* and HSC
959 regulators (**l**) *Cxcr4*, (**m**) *Dek*, (**n**) *Gpr56* and (**o**) *Ctnnb1* are upregulated in LR-HSCs. Values related to single

960 cells and referred to DESeq-normalized and baselined log(FPKM). Data are plotted as average population
961 expression ±SD. In **b**, **g**, **h** data represent mean ± s.e.m and the statistical significance was assessed by
962 Student's *t-tests*. * $p < 0.05$. $n = 4$ biological repeats. Scale bars, 10 µm (**a**).
963
964
965 **Supplementary Figure 7: Endothelial Jag2 maintains aged LR-HSCs at sinusoids.**

966 **a**, Relative frequency of endothelial and Nes-GFP^{low} cells expressing Jag2 in BM of young and old Nes-GFP
967 mice (n = 2-5). **b**, IF images showing Jag1 expression (red) in sinusoidal vessels (blue) and Nes-GFP^{low} cells
968 (green) in BM from young and old Nes-GFP mice. DAPI (white). **c**, Overview of the *in vitro* co-culture
969 experiments with blocking endothelial-derived Jag2. **d**, Epifluorescence images showing co-culture of YFP^{+}
970 HSCs (green) and endothelial cells. Scale bars, 20µm (**d***i*); zoomed inset 10 µm (**d***ii*). **e**, Number of YFP^{+} HSCs
971 after treatment with Jag2 blocking antibody and with isotype control. YFP^{+} HSCs samples were either assayed
972 in co-culture with freshly prepared endothelial cells or alone (n = 6-3). **f**, Representative FACS dot plots of the
973 gating strategy for YFP^{+} HSCs *in vitro* co-culture experiments with endothelial cells and blocking antibody
974 Jag2. **g**, Z-Stacked confocal whole-mount images of femoral BM from mouse treated with Jag2 blocking
975 antibody or isotype control. Samples were stained with the same secondary antibody (red). Vessels are stained
976 with CD31 and CD144 (blue). **h**, Pie charts depicting percentage of Ki-67^{+} and Ki-67^{-} HSCs present in distal-
977 diaphyseal-femoral central BM whole-mount images of Jag2 blocking antibody and isotype control
978 antibody treated mice (n = 966 and n = 109 HSCs per group from 3 images). **i**, Representative 3D
979 reconstruction of confocal whole-mount images showing sinusoidal (blue) location of Ki-67^{+} (red dots) and
980 Ki-67^{-} (yellow dots) HSCs present in distal-diaphyseal-femoral central BM of Jag2 blocking antibody treated
981 mice (1 unit = 45.72 µm). **j**, Percentage of Ki-67^{+} HSCs adjacent to sinusoids (< 10 µm) in distal-diaphyseal-
982 femoral central BM whole-mount images in BM of mice treated with Jag2 blocking antibody and isotype
983 control antibody (n = 472 and n = 28 HSCs from 3 areas per group). **k**, Percentage of clustered HSCs adjacent
984 to sinusoids (< 10 µm) in distal-diaphyseal-femoral central BM whole-mount images of mice treated with Jag2
985 blocking antibody and isotype control antibody (n = 653 and n = 28 HSCs from 4 and 3 areas). Data represent
986 mean ± s.e.m. In **a, e, j, k** the statistical significance was assessed by Student's *t-tests*. n = 2-6 biological

987 repeats. Scale bars, 20 µm (**b**), 10 µm (**d***i*), 10 µm (**d***ii*), 50 µm (**g**).

988

989 **Supplementary Figure 8: Impairment of the sinusoidal niche after 5-FU administration.**

990 **a**, Overview of the 5-FU experimental layout. **b**, Confocal images of 5-FU treated young femoral mice BM
991 show cycling Ki-67^{+} (green) CD150^{+} (red) CD41 CD48 Lin^{+} (white) clusters of MPPs. **c**, Experimental layout
992 of transplantation of aged YFP^{+} HSCs in young *Rag2*$^{-/-}$*γc*$^{-/-}$*Kit*$^{W/Wv}$ recipient mice and 5-FU administration. **d**,
993 Red blood cell count (RBC), myeloid (Gr1+, Mac1+), B cell (B220) and T cell (CD3) frequencies in PB of 5-
994 FU treated young and old mice (*n* = 12 mice each group). **e**, Cartoon scheme depicting experiments with
995 transplantations of 5-FU preconditioned, lethally irradiated (11 Gy) and control young and aged recipient mice
996 with young or old YFP^{+} donor HSCs. **f**, Percentage of engraftment from YFP^{+} HSCs in peripheral blood of
997 young and aged control and 5-FU preconditioned recipient mice (*n* = 4-6 mice per group). **g**, Quantification of
998 BV diameter and per volume in stacked images in central BM (≥ 50 µm from endost) from 5-FU treated (30d)
999 and non-treated young and old mice (*n* = 135/162/151/142 BVs from 3 areas, two mice per group). **h**, Z-stacked
1000 whole-mount images showing vasculature (CD31/CD144) in long bones from young and old mice 30 days
1001 after 5-FU administration and non-treated controls. **i**, t-SNE representation of gene expression data of young
1002 and aged CD31^{+} endothelial cells. **j**, Heatmap of differentially expressed genes (FDR adjusted p-value < 0.1).
1003 Data shows log-transformed, size-factor normalized and batch corrected expression. **k**, Diffusion map
1004 representation of cell cycle states of young and aged CD31^{+} endothelial cells. Cell cycle partitioning was
1005 performed based on gene expression data. **l**, Pie charts depicting percentage of Ki-67^{+} and Ki-67^{-} HSCs present
1006 in long bone whole-mount images in BM of WT young and old mice 30 days after 5-FU administration (*n* =
1007 80 young HSCs and *n* = 156 old HSCs, 3 mice per group). **m**, Frequency of HSCs and LSKs among BM cells
1008 in control and 30-day-5-FU treated young and aged mice (*n* =6 mice per group). Data represent mean ± s.e.m.
1009 In **d** the statistical significance was assessed by two-way-ANOVA-test. In **f**, **g**, **m**, the statistical significance
1010 was assessed by Student's *t-tests*. * $p < 0.05$, ** $p < 0.01$, *** $p < 0.001$. Scale bars, 100 µm (**h**); 50 µm (**b**).

1011

1012 **Supplementary Figure 9: Summary cartoon scheme and gating strategies.**

1013 **a**, Cartoon scheme depicting alterations of the aged niches. Aged HSCs compared to young are located more
1014 distant to the endosteum, to megakaryocytes, to arterioles and to periarteriolar Nes-GFP^{high} cells but not to

1015 Nes-GFP^{low} cells and sinusoids. With ageing megakaryocytes are increased. Endothelial cells and
1016 endosteal/periarteriolar Nes-GFP^{high} cells are dramatically reduced. The anatomy and morphology of arteries
1017 and arterioles in the aged epiphysis is massively changed. The morphology, anatomy and numbers of
1018 diaphyseal vessels, which are comprised mainly of sinusoids, and perisinusoidal Nes-GFP^{low} cells are not
1019 affected by ageing. Also, a significant increase in the distance of aged HSCs from arterioles compared to young
1020 is detected. The data convey that the sinusoidal/Nes-GFP^{low} cells localization and structure are uniquely
1021 preserved upon ageing. LR-HSCs, which represent in aged mice the population of aged HSCs with the highest
1022 regenerative potential, cell polarity and with non-clustering phenotype, were exclusively found at sinusoidal
1023 niches. Importantly, Jag2 plays a functional role in the maintenance of proximity and quiescence of stem cells
1024 at sinusoids. **b**, Representative gating strategy for Nes-GFP high and low BM cells; **c**, Gating strategy for
1025 megakaryocytes; **d**, Gating strategy for endothelial cells; **e**, Gating strategy for PB cells. Representative
1026 example of B220, CD3, Mac-1 and Gr-1 staining profile of white blood cells from an aged C57Bl6 mouse
1027 (more than 100-week-old).

1028 **Supplementary Table 1:** Total numbers of young and old HSCs in whole-mount images with endosteum and
1029 numbers of young and old HSCs residing in the endosteal area (< 50 µm to the endosteal surface).

1030 **Supplementary Table 2:** Total numbers of young and old HSCs in Ki-67 stained whole-mount images and
1031 numbers of young and old HSCs and numbers of Ki-67^{+} young and Ki-67^{+} old HSCs < 50 µm distant to
1032 vasculature, in the endosteal area (< 50 µm to the endosteal surface), in proximity to sinusoids (< 10 µm), in
1033 proximity to arterioles/arteries (< 10 µm) and in proximity to megakaryocytes (< 10 µm) and numbers of HSCs
1034 overlapping with more niches.

1035

1036 **Supplementary Table 3: Genes upregulated in aLR-HSCs compared to anLR-HSCs.** Genes are listed up
1037 to 3.0 fold change (FC). The p-value is also indicated alongside.

1038

1039 **Supplementary Table 4: Differentially expressed genes between young and aged CD31^{+} cells.** Genes are
1040 listed up to a FDR adjusted p-value of 0.25 (padj < 0.10 considered significant).

1041

1042 **Supplementary Video 1**: **Old LR-HSC in proximity to a sinusoid.**

1043 3D reconstruction of confocal high resolution whole-mount images of DOX treated old SCL-tTAxH2B-GFP
1044 humeral BM showing a single phenotypic $CD150^+$ (red) $CD41^-$ $CD48^-$ Lin^- (white) HSC in proximity to a
1045 sinusoidal vessel (FABP4, magenta). H2B-GFP^+ nuclei (green).

1046

1047 **Supplementary Video 2**: **Young HSC in physical association to an arteriole.**

1048 3D reconstruction of confocal high resolution whole-mount images of young femoral WT BM showing a single
1049 phenotypic $CD150^+$ (red) $CD41^-$ $CD48^-$ Lin^- (white) HSC in physical association to an arteriole (CD31 and
1050 CD144, blue).

1051

1052 **Supplementary Video 3**: **Old HSCs are located distant to arterioles.**

1053 3D reconstruction of confocal high resolution whole-mount images of old femoral WT BM showing two
1054 phenotypic $CD150^+$ (red) $CD41^-$ $CD48^-$ Lin^- (white) HSCs located distant to an arteriole (CD31 and CD144,
1055 blue). Yellow line marks the arteriolar vessel.

1056

1057 **Supplementary Video 4**: **Young HSC in proximity to a sinusoid.**

1058 3D reconstruction of confocal high resolution whole-mount images of young femoral WT BM showing a single
1059 phenotypic $CD150^+$ (red) $CD41^-$ $CD48^-$ Lin^- (white) HSC in proximity to a sinusoidal vessel (CD31 and
1060 CD144, blue).

1061

1062 **Supplementary Video 5**: **Old HSCs adjacent to a sinusoidal vessel.**

1063 3D reconstruction of confocal high resolution whole-mount images of old femoral WT BM showing two
1064 phenotypic $CD150^+$ (red) $CD41^-$ $CD48^-$ Lin^- (white) HSCs in proximity to a sinusoidal vessel (CD31 and
1065 CD144, blue)

1066

1067 **Supplementary Video 6**: **Old perisinusoidal LRC in proximity to a sinusoidal $Jag2^+$ cell**

1068 3D reconstruction of confocal high resolution whole-mount images of DOX treated old SCL-tTAxH2B-GFP

1069 humeral BM showing a single H2B-GFP^{+} LRC (green) in proximity to a Jag2^{+} cell (red) at a sinusoidal vessel

1070 (FABP4, blue).

Data availability

All data generated or analysed during this study are included in this published article (and its supplementary information files) or are available from the corresponding author on reasonable request. RNA sequencing data are available at GEO under the accession code: XXXX (accession codes will be available before publication).

Code availability

Code and algorithm generated during this study are included in this published article (and its supplementary information files) or are available from the corresponding author on reasonable request.

Ethical compliance for mouse experiments

All mouse experiments were performed in compliance with the ethical regulations according to the German Law for Welfare of Laboratory Animals and were approved by the Institutional Review Board of the Ulm University as well as by the Regierungspraesidium Tuebingen (state government of Baden-Württemberg).

Figure 1:

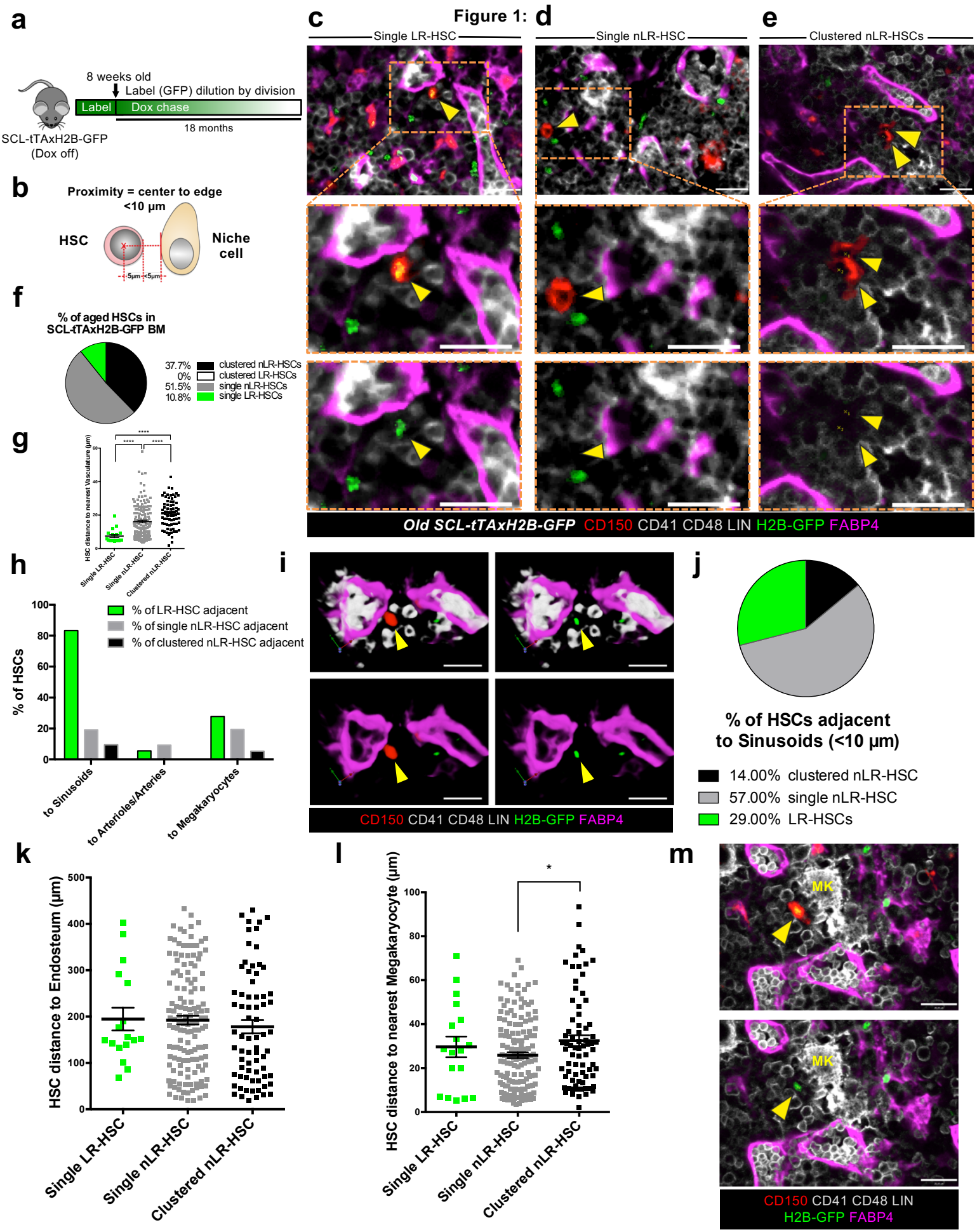
a
8 weeks old
Label (GFP) dilution by division
Label
Dox chase
18 months
SCL-tTAxH2B-GFP
(Dox off)
b
Proximity = center to edge
<10 µm
HSC
Niche cell
5µm
<5µm
c
Single LR-HSC
d
Single nLR-HSC
e
Clustered nLR-HSCs
Old SCL-tTAxH2B-GFP CD150 CD41 CD48 LIN H2B-GFP FABP4
f
% of aged HSCs in SCL-tTAxH2B-GFP BM
37.7% clustered nLR-HSCs
0% clustered LR-HSCs
51.5% single nLR-HSCs
10.8% single LR-HSCs
g
HSC distance to nearest Vasculature (µm)
Single LR-HSC
Single nLR-HSC
Clustered nLR-HSC
h
% of HSCs
% of LR-HSC adjacent
% of single nLR-HSC adjacent
% of clustered nLR-HSC adjacent
to Sinusoids
to Arterioles/Arteries
to Megakaryocytes
i
CD150 CD41 CD48 LIN H2B-GFP FABP4
j
% of HSCs adjacent to Sinusoids (<10 µm)
14.00% clustered nLR-HSC
57.00% single nLR-HSC
29.00% LR-HSCs
k
HSC distance to Endosteum (µm)
Single LR-HSC
Single nLR-HSC
Clustered nLR-HSC
l
HSC distance to nearest Megakaryocyte (µm)
*
Single LR-HSC
Single nLR-HSC
Clustered nLR-HSC
m
MK
MK
CD150 CD41 CD48 LIN
H2B-GFP FABP4

Figure 2:

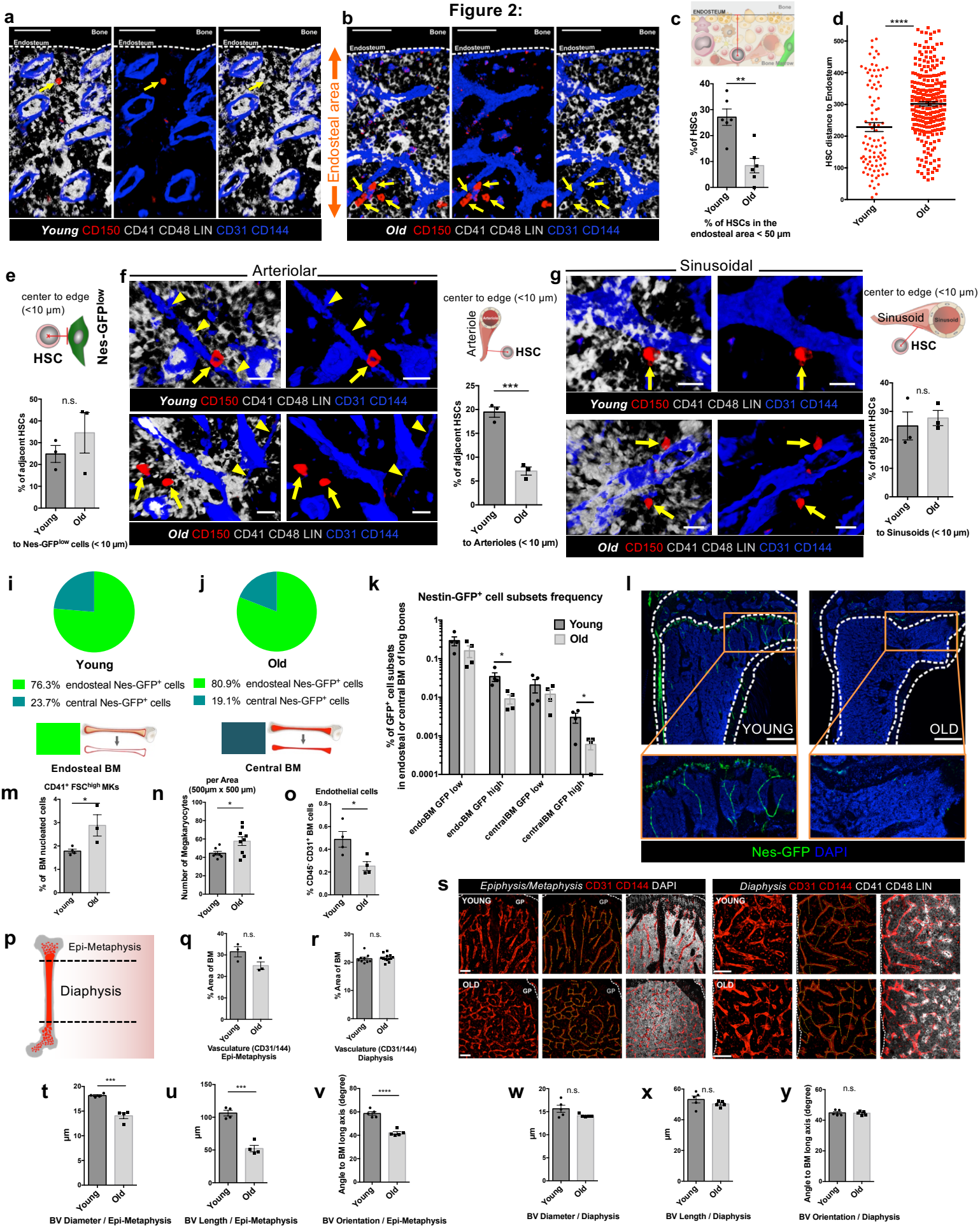
a
Bone
Endosteum
Young CD150 CD41 CD48 LIN CD31 CD144
b
Endosteal area
Old CD150 CD41 CD48 LIN CD31 CD144
c
ENDOSTEUM
Bone
Bone Marrow
% of HSCs
Young
Old
% of HSCs in the endosteal area < 50 µm
d
HSC distance to Endosteum
e
center to edge (<10 µm)
HSC
Nes-GFP low
% of adjacent HSCs
n.s.
to Nes-GFP low cells (< 10 µm)
f
Arteriolar
Young CD150 CD41 CD48 LIN CD31 CD144
Old CD150 CD41 CD48 LIN CD31 CD144
Arteriole
to Arterioles (< 10 µm)
g
Sinusoidal
Sinusoid
to Sinusoids (< 10 µm)
i
Young
76.3% endosteal Nes-GFP+ cells
23.7% central Nes-GFP+ cells
j
Old
80.9% endosteal Nes-GFP+ cells
19.1% central Nes-GFP+ cells
Endosteal BM
Central BM
k
Nestin-GFP+ cell subsets frequency
Young
Old
% of GFP+ cell subsets in endosteal or central BM of long bones
endoBM GFP low
endoBM GFP high
centralBM GFP low
centralBM GFP high
l
YOUNG
OLD
Nes-GFP DAPI
m
CD41+ FSChigh MKs
% of BM nucleated cells
n
per Area (500µm x 500 µm)
Number of Megakaryocytes
o
Endothelial cells
% CD45- CD31+ BM cells
p
Epi-Metaphysis
Diaphysis
q
% Area of BM
Vasculature (CD31/144) Epi-Metaphysis
r
Vasculature (CD31/144) Diaphysis
s
Epiphysis/Metaphysis CD31 CD144 DAPI
Diaphysis CD31 CD144 CD41 CD48 LIN
YOUNG
OLD
GP
t
µm
BV Diameter / Epi-Metaphysis
u
BV Length / Epi-Metaphysis
v
Angle to BM long axis (degree)
BV Orientation / Epi-Metaphysis
w
BV Diameter / Diaphysis
x
BV Length / Diaphysis
y
BV Orientation / Diaphysis

Figure 3:

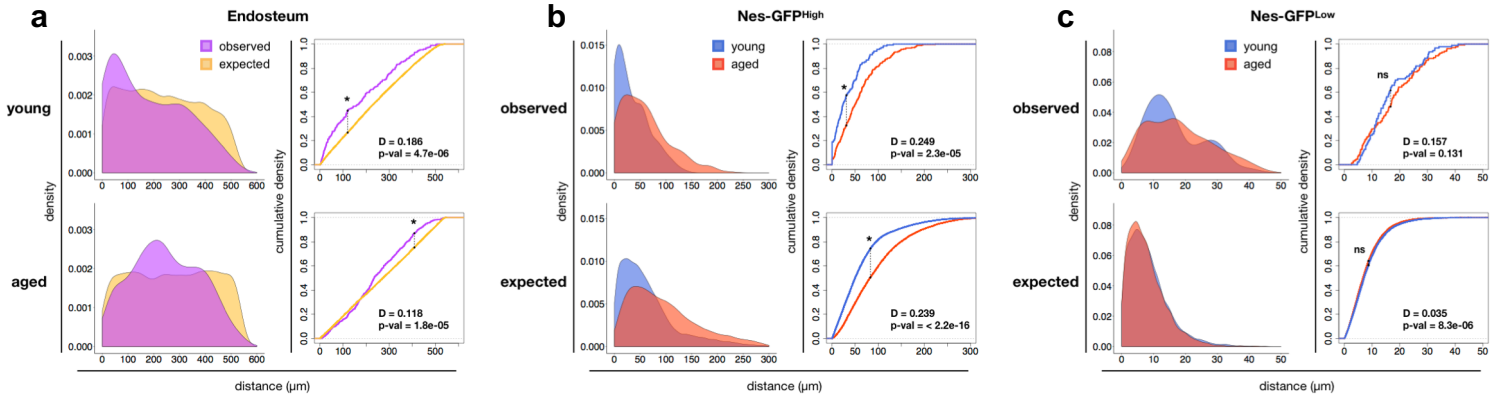

d

Niche type	Change in distance of HSCs upon aging	
	Histology	In-silico model
Endosteum	↑	↑
Nes-GFP^{high}	↑	↑
Nes-GFP^{low}	=	=
CD41^{+} MKs	↑	=

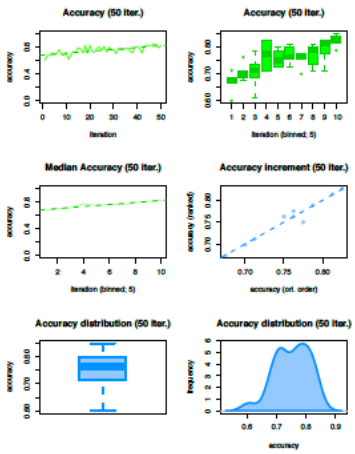

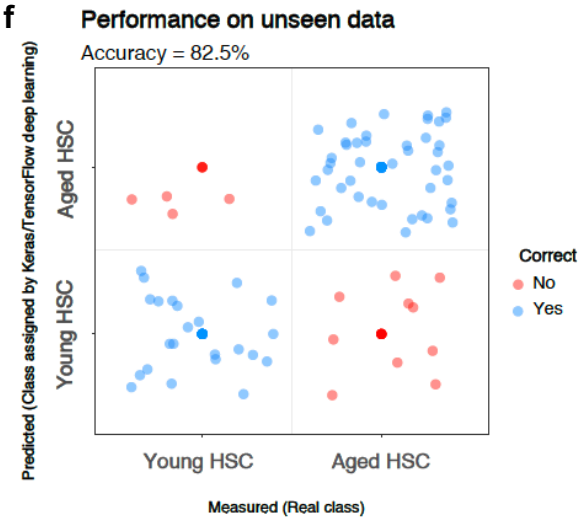

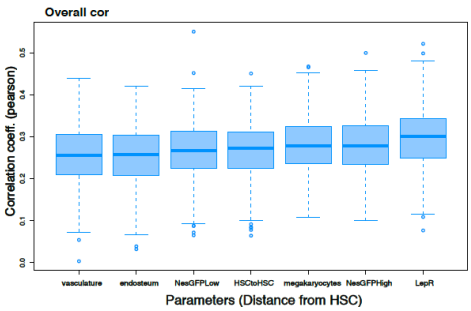

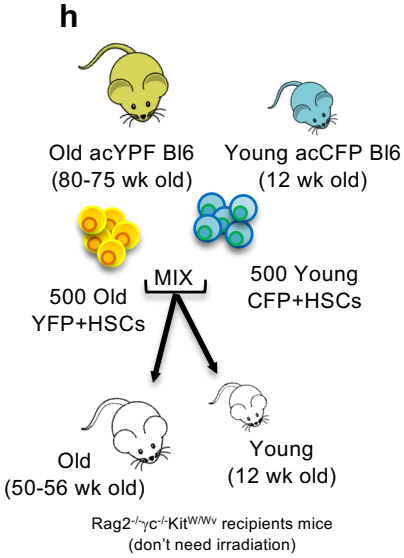

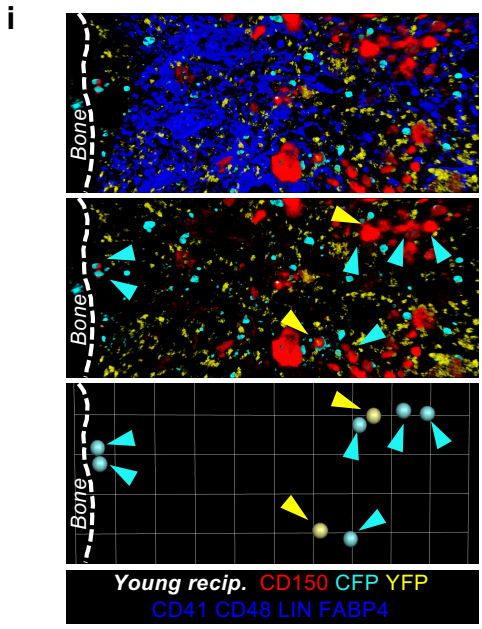

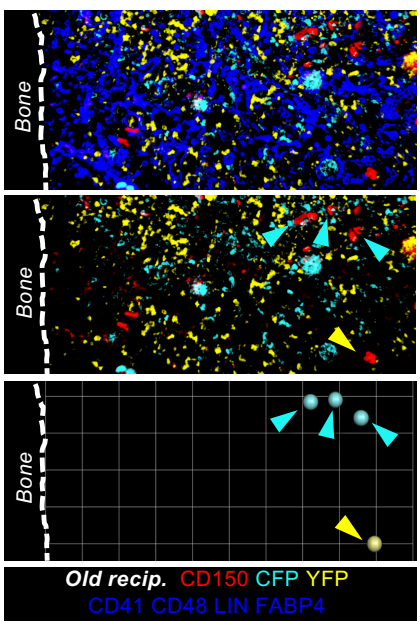

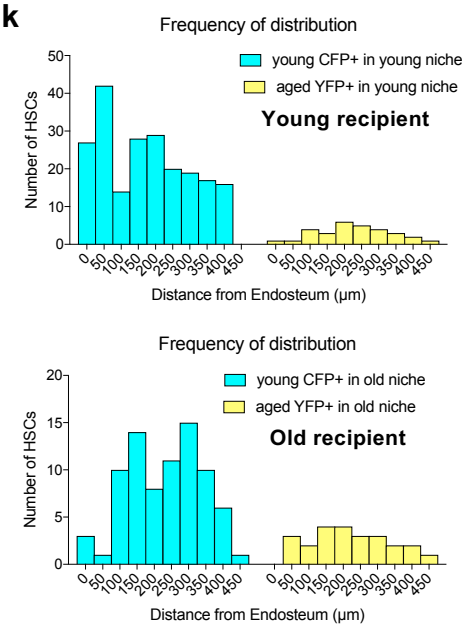

Figure 4:

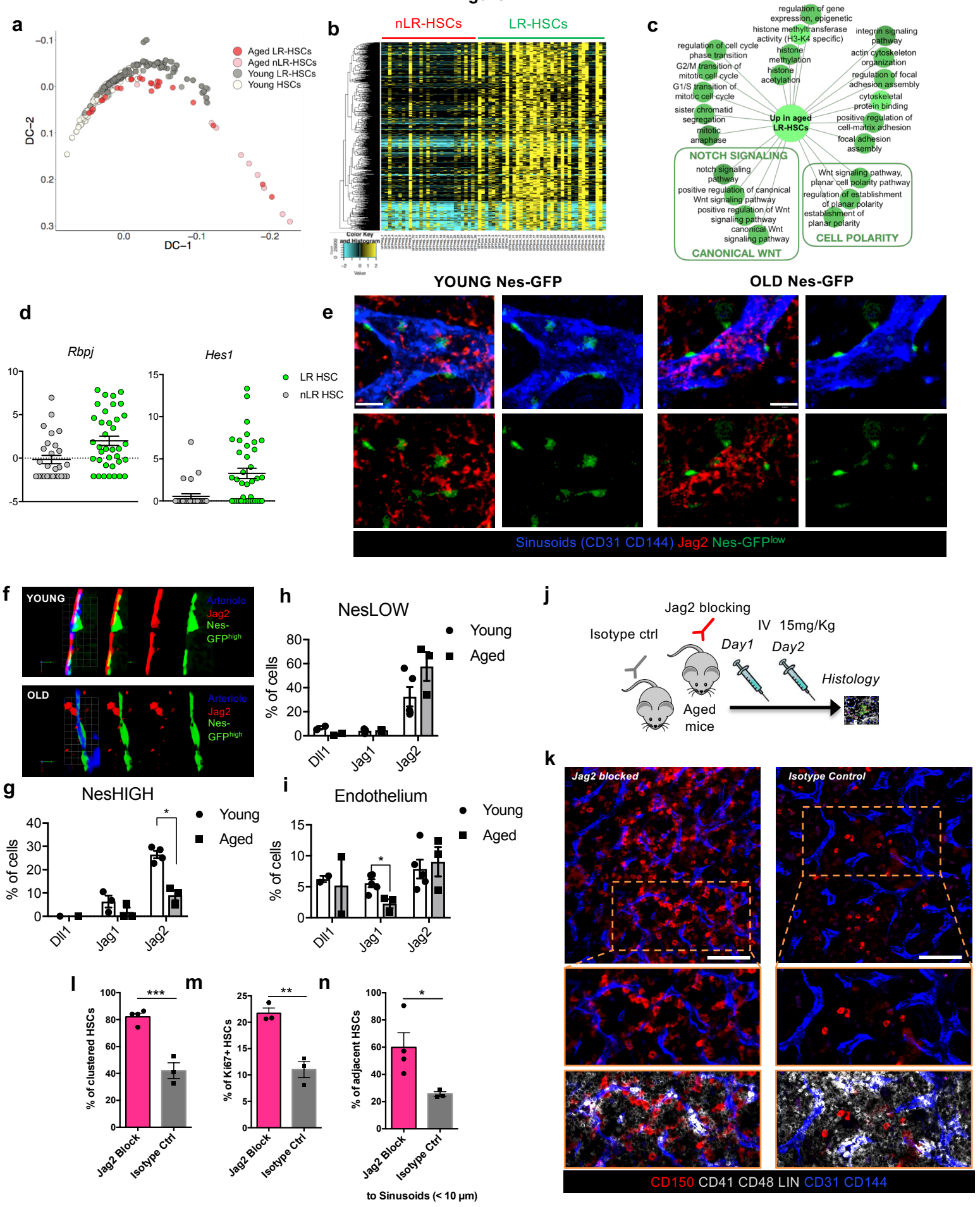
a
Aged LR-HSCs
Aged nLR-HSCs
Young LR-HSCs
Young HSCs
DC−2
DC−1
b
nLR-HSCs
LR-HSCs
Color Key and Histogram
c
regulation of gene expression, epigenetic
histone methyltransferase activity (H3-K4 specific)
integrin signaling pathway
regulation of cell cycle phase transition
histone methylation
actin cytoskeleton organization
G2/M transition of mitotic cell cycle
histone acetylation
regulation of focal adhesion assembly
G1/S transition of mitotic cell cycle
cytoskeletal protein binding
sister chromatid segregation
Up in aged LR-HSCs
positive regulation of cell-matrix adhesion
mitotic anaphase
focal adhesion assembly
NOTCH SIGNALING
notch signaling pathway
positive regulation of canonical Wnt signaling pathway
positive regulation of Wnt signaling pathway
canonical Wnt signaling pathway
CANONICAL WNT
Wnt signaling pathway, planar cell polarity pathway
regulation of establishment of planar polarity
establishment of planar polarity
CELL POLARITY
d
Rbpj
Hes1
LR HSC
nLR HSC
e
YOUNG Nes-GFP
OLD Nes-GFP
Sinusoids (CD31 CD144) Jag2 Nes-GFPlow
f
YOUNG
Arteriole
Jag2
Nes-GFPhigh
OLD
Arteriole
Jag2
Nes-GFPhigh
h
NesLOW
Young
Aged
% of cells
Dll1
Jag1
Jag2
g
NesHIGH
Young
Aged
% of cells
Dll1
Jag1
Jag2
i
Endothelium
Young
Aged
% of cells
Dll1
Jag1
Jag2
j
Jag2 blocking
Isotype ctrl
IV 15mg/Kg
Day1
Day2
Histology
Aged mice
k
Jag2 blocked
Isotype Control
CD150 CD41 CD48 LIN CD31 CD144
l
% of clustered HSCs
Jag2 Block
Isotype Ctrl
m
% of Ki67+ HSCs
Jag2 Block
Isotype Ctrl
n
% of adjacent HSCs
Jag2 Block
Isotype Ctrl
to Sinusoids (< 10 µm)

Figure 5:

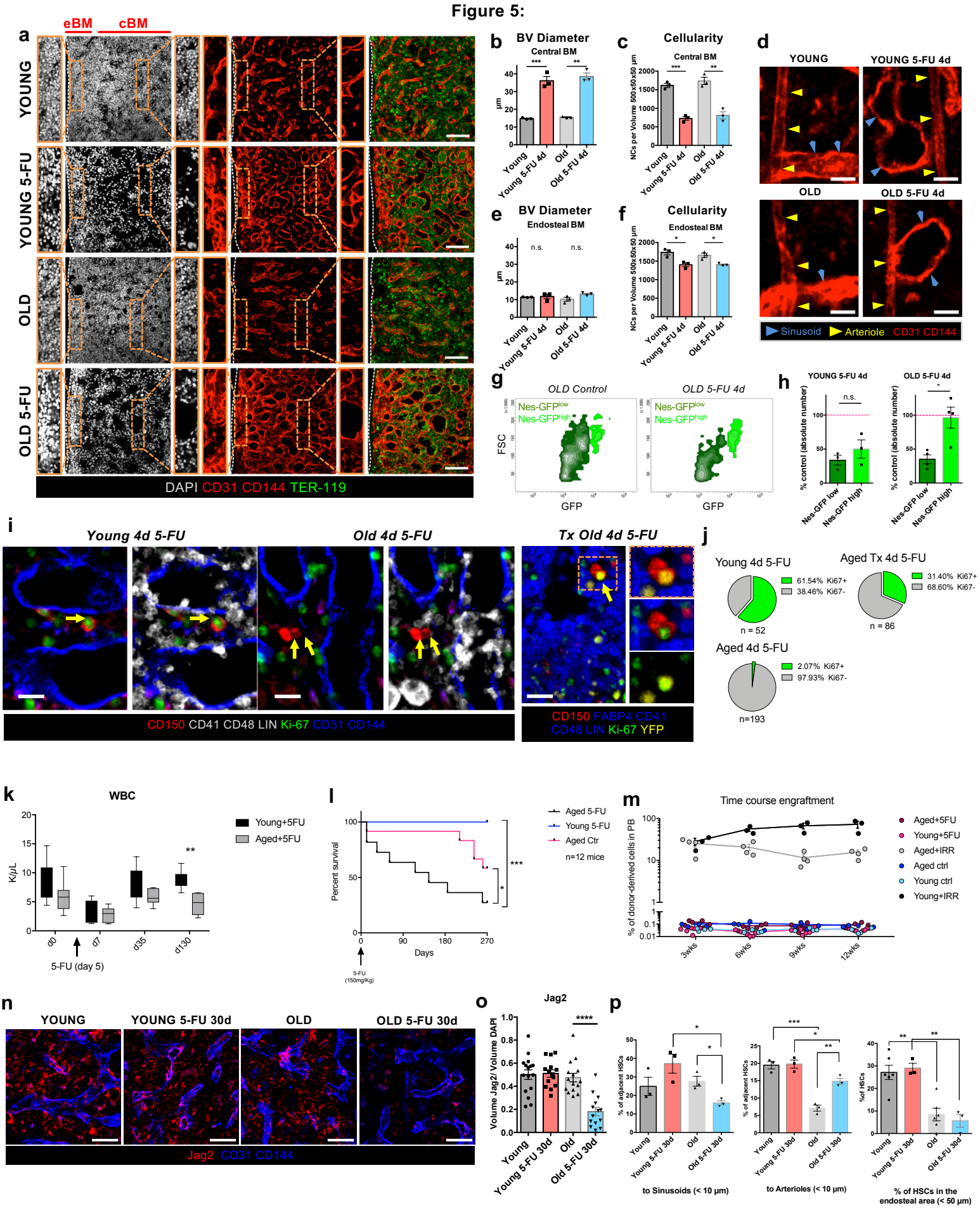
a
eBM
cBM
YOUNG
YOUNG 5-FU
OLD
OLD 5-FU
DAPI CD31 CD144 TER-119
b
BV Diameter
Central BM
µm
Young
Young 5-FU 4d
Old
Old 5-FU 4d
c
Cellularity
Central BM
NCs per Volume 500x50x50 µm
d
YOUNG
YOUNG 5-FU 4d
OLD
OLD 5-FU 4d
Sinusoid
Arteriole
CD31 CD144
e
BV Diameter
Endosteal BM
n.s.
f
Cellularity
Endosteal BM
NCs per Volume 500x50x50 µm
g
OLD Control
OLD 5-FU 4d
Nes-GFPlow
Nes-GFPhigh
FSC
GFP
h
YOUNG 5-FU 4d
OLD 5-FU 4d
% control (absolute number)
Nes-GFP low
Nes-GFP high
i
Young 4d 5-FU
Old 4d 5-FU
Tx Old 4d 5-FU
CD150 CD41 CD48 LIN Ki-67 CD31 CD144
CD150 FABP4 CD41
CD48 LIN Ki-67 YFP
j
Young 4d 5-FU
61.54% Ki67+
38.46% Ki67-
n = 52
Aged Tx 4d 5-FU
31.40% Ki67+
68.60% Ki67-
n = 86
Aged 4d 5-FU
2.07% Ki67+
97.93% Ki67-
n=193
k
WBC
K/µL
Young+5FU
Aged+5FU
d0
d7
d35
d130
5-FU (day 5)
l
Percent survival
Days
5-FU (150mg/Kg)
Aged 5-FU
Young 5-FU
Aged Ctr
n=12 mice
m
Time course engraftment
% of donor-derived cells in PB
3wks
6wks
9wks
12wks
Aged+5FU
Young+5FU
Aged+IRR
Aged ctrl
Young ctrl
Young+IRR
n
YOUNG
YOUNG 5-FU 30d
OLD
OLD 5-FU 30d
Jag2 CD31 CD144
o
Jag2
Volume Jag2/ Volume DAPI
Young
Young 5-FU 30d
Old
Old 5-FU 30d
p
% of adjacent HSCs
to Sinusoids (< 10 µm)
to Arterioles (< 10 µm)
% of HSCs
% of HSCs in the endosteal area (< 50 µm)